RESEARCH ARTICLE

Unique structural features in an Nramp metal transporter impart substrate-specific proton cotransport and a kinetic bias to favor import

Aaron T. Bozzi, Lukas B. Bane, Christina M. Zimanyi, and Rachelle Gaudet⬤

Natural resistance-associated macrophage protein (Nramp) transporters enable uptake of essential transition metal micronutrients in numerous biological contexts. These proteins are believed to function as secondary transporters that harness the electrochemical energy of proton gradients by "coupling" proton and metal transport. Here we use the *Deinococcus radiodurans* (Dra) Nramp homologue, for which we have determined crystal structures in multiple conformations, to investigate mechanistic details of metal and proton transport. We untangle the proton-metal coupling behavior of DraNramp into two distinct phenomena: ΔpH stimulation of metal transport rates and metal stimulation of proton transport. Surprisingly, metal type influences substrate stoichiometry, leading to manganese-proton cotransport but cadmium uniport, while proton uniport also occurs. Additionally, a physiological negative membrane potential is required for high-affinity metal uptake. To begin to understand how Nramp's structure imparts these properties, we target a conserved salt-bridge network that forms a proton-transport pathway from the metal-binding site to the cytosol. Mutations to this network diminish voltage and ΔpH dependence of metal transport rates, alter substrate selectivity, perturb or eliminate metal-stimulated proton transport, and erode the directional bias favoring outward-to-inward metal transport under physiological-like conditions. Thus, this unique salt-bridge network may help Nramp-family transporters maximize metal uptake and reduce deleterious back-transport of acquired metals. We provide a new mechanistic model for Nramp proton-metal cotransport and propose that functional advantages may arise from deviations from the traditional model of symport.

Introduction

Cells commit significant ATP expenditure to maintain ionic gradients across membranes, a form of energy storage. Selective membrane permeability also generates a stable charge imbalance that produces a membrane voltage, generally negative. Secondary transporters harness these electrochemical gradients by coupling the energetically favorable movement of abundant ions (Na⁺, K⁺, H⁺, and Cl⁻) to the (often uphill) movement of substrates (Gadsby, 2009; Forrest et al., 2011; Shilton, 2015; LeVine et al., 2016). Symporters move primary substrate and driving ions in the same direction through an alternating-access mechanism in which only the empty or fully loaded transporter can easily undergo conformational change (Fig. 1 A). Large-magnitude kinetic barriers preclude conformational change for transporters bound to a single species and thus prevent uniport events (Fig. 1 B): "futile cycles" that dissipate the driving ion gradients and, even more deleterious, the back transport of the primary substrate down its concentration gradient (LeVine

et al., 2016; Henderson et al., 2019). These secondary transporters' structures thus evolved to enforce a codependence or "coupling" between primary substrate and driving ions, such that both must simultaneously bind for transport to occur (Boudker and Verdon, 2010; Forrest et al., 2011).

The natural resistance-associated macrophage protein (Nramp) family of transporters imports divalent transition metal ions, essential micronutrients serving as cofactors to myriad metabolic enzymes. Prokaryotic Nramps perform high-affinity Mn²⁺ scavenging (Ma et al., 2009; Cellier, 2012), while in eukaryotes, including humans, Nramps are essential to iron dietary uptake, iron trafficking to and recycling from erythrocytes, and the metal-withholding innate immune defense (Andrews, 2008; Hood and Skaar, 2012; Abbaspour et al., 2014; Coffey and Ganz, 2017). Nramps are promiscuous with regard to metal substrate identity: while Mn²⁺ and/or Fe²⁺ are typically the physiological substrates (Supek et al., 1996; Fleming et al.,

Department of Molecular and Cellular Biology, Harvard University, Cambridge, MA.

Correspondence to Rachelle Gaudet: gaudet@mcb.harvard.edu; A.T. Bozzi's present address is Department.of Chemistry, Massachusetts Institute of Technology, Cambridge, MA; L.B. Bane's present address is D. E. Shaw Research, New York, NY; C.M. Zimanyi's present address is New York Structural Biology Center, New York, NY.
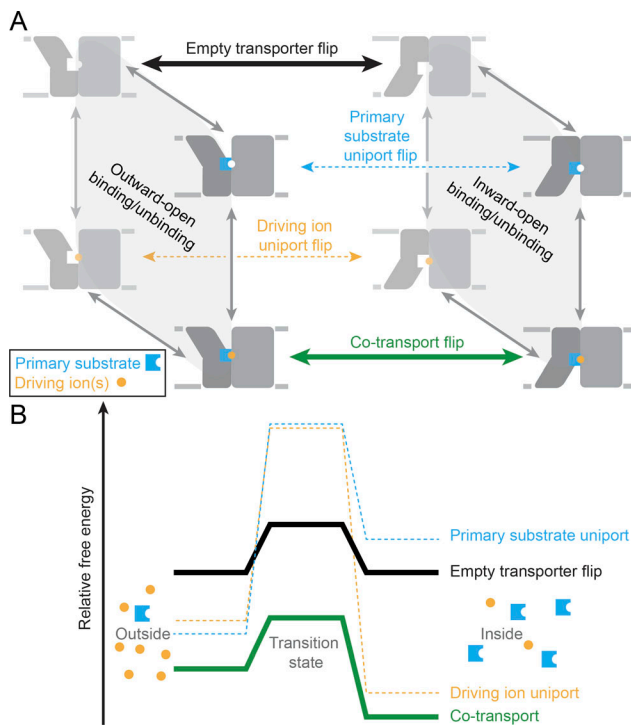
Figure 1. **Kinetic model of canonical symport. (A)** Transport cycle diagram illustrating all possible binding/unbinding/transport events for a canonical symporter. **(B)** Free energy diagrams for transport events. For a tightly coupled (canonical) symporter, essentially insurmountable kinetic barriers in the protein's free energy landscape prevent uniport events (dashed lines). Thus, only the empty or fully loaded transporter (solid lines) can efficiently convert from outward-open to inward-open (or vice versa). The combined electrochemical gradients of the primary substrate and the driving ions determine the net direction of cotransport, with a typical physiological situation for symport displayed here (higher concentration of primary substrate inside and higher concentration of driving ion outside).

1997; Gunshin et al., 1997; Kehres et al., 2000; Makui et al., 2000; Thomine et al., 2000; Cailliatte et al., 2010), Nramps also transport the biologically useful metals Co^{2+}, Ni^{2+}, and Zn^{2+} (Picard et al., 2000; Mackenzie et al., 2006; Illing et al., 2012; Ehrnstorfer et al., 2014) as well as the toxic heavy metals Cd^{2+}, Pb^{2+}, and Hg^{2+} (Bannon et al., 2002; Bressler et al., 2004; Vázquez et al., 2015).

Given typically low environmental metal ion concentrations, a coupling mechanism to a driving ion may be required to make metal uptake thermodynamically favorable. In the seminal functional study with rat Nramp2 expressed in oocytes, Gunshin et al. (1997) demonstrated both that low external pH greatly accelerates Fe^{2+} transport and that extracellular Fe^{2+} stimulates H^+ entry. These and similar findings with other homologues (Chen et al., 1999; Tandy et al., 2000; Xu et al., 2004; Mackenzie et al., 2007; Ehrnstorfer et al., 2017) support Nramp's designation as a symporter that couples proton entry to transition metal uptake (Mackenzie and Hediger, 2004; Courville et al., 2006; Nevo and Nelson, 2006; Cellier, 2012; Shawki et al., 2012). However, strict thermodynamic coupling, such that a gradient of one substrate clearly drives uphill transport of the other, between

metal and proton cosubstrates has yet to be demonstrated. In addition, electrophysiological studies of Nramps showed variable proton–metal transport stoichiometries depending on pH and membrane potential (Chen et al., 1999; Nevo and Nelson, 2004), as well as significant proton uniport (Gunshin et al., 1997; Chen et al., 1999; Xu et al., 2004; Mackenzie et al., 2006, 2007; Shawki and Mackenzie, 2010; Bozzi et al., 2019), which suggests loose coupling (Nelson et al., 2002; Henderson et al., 2019). Furthermore, multiple Nramp homologues exhibit a pronounced voltage dependence of metal transport rate (Gunshin et al., 1997; Chen et al., 1999; Xu et al., 2004; Mackenzie et al., 2007).

Crystal structures of prokaryotic Nramp homologues revealed a LeuT-fold (Ehrnstorfer et al., 2014), which is second most common among secondary transporters (Forrest et al., 2011; Shi, 2013), and an alternating-access conformational cycle (Bozzi et al., 2016b, 2019; Ehrnstorfer et al., 2017). These structures and associated mutagenesis studies revealed the large-scale intramolecular rearrangements required for metal transport (Bozzi et al., 2016b, 2019; Ehrnstorfer et al., 2017), the conserved residues that form the metal-binding site and enforce substrate selectivity (Ehrnstorfer et al., 2014; Bozzi et al., 2016a, 2019), and the Nramp-specific network of charged residues that enables proton flux through the outward-open state (Bozzi et al., 2019).

Here, using the *Deinococcus radiodurans* (Dra) Nramp homologue, for which we previously determined four distinct crystal structures (Bozzi et al., 2016b, 2019), we provide the first detailed in vitro investigation of Nramp metal and proton transport kinetics as a foundation to understand its unique, noncanonical transport mechanism. We find that a physiological negative voltage is required for efficient metal transport to occur, regardless of otherwise favorable metal and proton gradients. We further show that both low external pH and a favorable pH gradient accelerate metal transport, while added metal can in turn stimulate increased proton uptake. Surprisingly, voltage and pH dependence vary significantly based on metal elemental identity, as does the stoichiometry of proton–metal cotransport. (Note that we use "cotransport" to describe macroscopic observations of transport of both metal ions and protons, without a determination of whether these transport events are thermodynamically coupled, and "uniport" to describe macroscopic observations of transport of only metal ions or protons.) Using a large panel of mutations to the conserved residues implicated in metal binding and/or proton transport, we identify structural features that may contribute to the voltage and pH dependence of transport rates and facilitate proton–metal cotransport. We demonstrate that Nramp deviates significantly from the canonical model for symport (Fig. 1), such that proton–metal cotransport, metal uniport, and proton uniport can all occur. Finally, we show that forward metal transport by Nramp occurs much more readily than analogous back transport, regardless of the thermodynamic driving force. This suggests that evolution may have shaped Nramp's structure to enforce a transport mechanism in which a nearly insurmountable kinetic barrier prevents the loss of cytosolic metal stores.

Materials and methods

In vivo Co²⁺ transport

Co^{2+} transport in *Escherichia coli* was performed as described (Bozzi et al., 2016b, 2019). In brief, C41(DE3) cells expressing WT or mutant DraNramp or an empty vector were grown to $OD_{600} \approx$ 0.6 and induced with 0.1 mM isopropyl-β-D-thiogalactoside for 75 min. Cells were washed and aliquoted into 96-well plates at 37°C, and 200 µM $Co(NO_3)_2$ was added to initiate transport. After the desired time interval, an excess of EDTA was added to quench further uptake. Cells were then pelleted and washed three times before resuspension in 1% $(NH_4)_2S$ to precipitate internal Co^{2+}. The black precipitated cobalt sulfide darkened cell pellets, allowing quantification of relative metal uptake. The assay buffer was 50 mM HEPES, pH 7.0, 60 mM NaCl, 10 mM KCl, 0.5 mM $MgCl_2$, and 0.216% glucose. For the varied $[K^+]$ measurements, the assay buffer was 50 mM HEPES, pH 7.0, 60 mM NaCl, 0.5 mM $MgCl_2$, X mM KCl, and $(82.5 - X)$ mM choline chloride, with X indicated in the corresponding figure legends. For each biological replicate reported in the figure legends, a separate culture of transformed *E. coli* was grown and induced to express the heterologous Nramp construct.

Cysteine accessibility measurements

Cysteine accessibility measurements in *E. coli* were performed as described (Bozzi et al., 2016b, 2019), except that the assay buffer used was the same as for the Co^{2+} transport experiments. In brief, cells expressing single-cysteine Nramp constructs were grown and aliquoted into 96-well plates as above. Varying concentrations (twofold dilutions) of *N*-ethylmaleimide (NEM) were added to different wells for 15 min at room temperature (RT) to label accessible cysteines before quenching with excess free cysteine. Cells were then lysed in 6 M urea, 0.1% SDS, and 0.5 mM dithiothreitol (DTT), and an excess (2 mM) of 5K-polyethylene glycol maleimide was added to modify any previously protected cysteines. Samples were analyzed by SDS-PAGE and Western blot using an anti-His fluorescent antibody (Qiagen) to determine the proportion of protein in the normal-weight and 5K-polyethylene glycol–shifted bands. For each biological replicate reported in the figure legends, a separate culture of transformed *E. coli* was grown and induced to express the heterologous Nramp construct.

Cloning, expression, and purification of DraNramp constructs for proteoliposome assays

DraNramp constructs were cloned, expressed, and purified as described (Bozzi et al., 2019), with the following changes: protein was purified from cell pellets in a single day and washed/eluted from Ni-NTA agarose resin in buffers with 0.03% *n*-dodecyl-β-D-maltopyranoside. Proteins were concentrated and buffer exchanged into 100 mM NaCl, 10 mM HEPES, pH 7.5, and 0.1% *n*-decyl-β-D-maltopyranoside on a PD10 desalting column, with final protein concentrations normalized to 1.2 mg/ml and aliquots flash frozen in liquid nitrogen. Single-cysteine constructs A53C and A61C were purified in the presence of 1 mM DTT.

Proteoliposome preparation

A 75:25 wt/wt mixture of 1-palmitoyl-2-oleoyl-sn-glycero-3-phosphoethanolamine and 1-palmitoyl-2-oleoyl-sn-glycero-3-phosphoglycerol in chloroform (Avanti Polar Lipids) was dried under nitrogen in a warm water bath, redissolved in pentane, and dried again. Lipids were resuspended at 20 mg/ml in 5 mM *n*-decyl-β-D-maltopyranoside in reconstitution buffer (typically ~90 mM KCl, 30 mM NaCl, and either 10 mM MOPS, pH 7.0 [or 10 mM Mes, pH 6.0, for pH 6.0 inside] for Fura-2 metal transport experiments or 0.5 mM MOPS, pH 7.0 for proton transport or side-by-side proton and metal transport experiments). Protein was added at a 1:400 wt/wt ratio to lipid, and the mixture was dialyzed at 4°C to remove the detergent in 10-kD molecular weight cutoff dialysis cassettes against reconstitution buffer with 0.2 mM EDTA for 1 d, then with 0.1 mM EDTA for 1–3 d, then overnight at RT against reconstitution buffer. For A53C and A61C, 1 and 0.5 mM DTT was included in the first two dialysis steps. Fluorescent dye (either 1:49 vol/vol 5 mM Fura-2 pentapotassium salt or 1:66 vol/vol 10 mM 2′,7′-bis(carboxyethyl)-5(6)-carboxyfluorescein [BCECF] in dimethyl sulfoxide) was incorporated into proteoliposomes permeabilized by three freeze–thaw cycles in dry ice–ethanol and RT water baths (and sometimes stored at –80°C after the third freeze). Proteoliposomes were extruded through a 400-nM filter to create uniform-sized vesicles and buffer exchanged one to two times on a PD10 desalting column preequilibrated with NaCl or KCl/10 mM MOPS, pH 7.0 (or Mes, pH 6) buffer. Peak proteoliposome-containing fractions were pooled to remove unincorporated dye. DraNramp orients randomly during proteoliposome reconstitution, resulting in a 50:50 mixture of inside-out and outside-out transporters (Bozzi et al., 2019).

Proteoliposome transport assays and data analysis

Proteoliposomes loaded with either 100 µM Fura-2 or 150 µM BCECF were diluted into buffer containing appropriate [KCl] to establish the desired membrane potential and aliquoted into 96-well black clear-bottom plates. Following baseline fluorescence measurement, 5× metal (750 µM final concentration unless otherwise noted) and valinomycin (100 nM final concentration) were added. A fresh stock of 100 mM $FeSO_4$ in 100 mM L-ascorbic acid was made for each assay; stocks of 100 mM $CdCl_2$, $MnCl_2$, $ZnCl_2$, $Co(NO_3)_2$, and $CaCl_2$ were freshly diluted into appropriate NaCl or KCl buffer. For assays with a pH gradient, the metals were diluted into 100 mM Mes at pH 5.5, 5.8, 6.0, or 6.5 or MOPS at pH 7.2 with appropriate NaCl/KCl. The reported external pH upon metal addition was determined from proportional mixings of larger volumes of the same buffers. To premodify A61C constructs for transport assays, liposomes were diluted into 120 mM NaCl and 10 mM MOPS, pH 7.0, containing 3 mM 2-(trimethylammonium)ethyl methanethiosulfonate (MTSET) and incubated at least 30 min at RT before beginning transport assays. Metal transport was monitored by measuring Fura-2 fluorescence at $\lambda_{ex} = 340$ and 380 nm and $\lambda_{em} = 510$ nm. Proton transport was monitored by measuring BCECF fluorescence at $\lambda_{ex} = 450$ and 490 nm and $\lambda_{em} = 535$ nm. To calculate concentrations of imported metal, the Fura-2 340/380 ratio and experimentally determined K_d values (Grynkiewicz et al., 1985; Hinkle et al., 1992) were used for Ca^{2+} and Cd^{2+} as described previously (Bozzi et al., 2016a); the Ca^{2+} K_d value was used as an approximation for Zn^{2+}. For Mn^{2+}, Fe^{2+}, and Co^{2+}, the fraction

of Fura-2 340 and/or 380 fluorescence quenched, normalized to maximum observed quenching, was used to estimate imported metal. For proton uptake, the BCECF 450/490 ratio was used to calculate internal pH, which, along with the known total internal buffer (0.5 mM) and dye (150 µM) concentration, was used to calculate net proton import via the Henderson–Hasselbalch equation. Initial rates were calculated in Excel, and Michaelis–Menten parameters were fitted using Matlab. For some Mn^{2+} uptake traces (typically at low magnitude $\Delta\Psi$), a brief initial lag in uptake was observed, the origin of which remains unexplained at this time. For these traces, the first few data points were omitted when determining the transport rate. For each technical replicate reported in the figure legends, a separate aliquot of dye-loaded proteoliposomes was diluted into the appropriate outside buffer, including cysteine modifiers if applicable, and then fluorescence time course data were collected before and after the addition of valinomycin, metal substrate, and/or ionomycin. Note that for metal uptake measurements, the assay setup precludes an accurate measure of equilibrium internal metal concentration, as the Fura-2 concentration limits the maximum detectable signal, and Fura-2 likely acts as a thermodynamic sink for divalent cations. Therefore, transport rates were calculated from data before the Fura-2 signal reached 50% saturation.

Online supplemental material

Figs. S1, S2, S3, S5, S7, S8, S10, and S11 contain representative traces and controls for liposome metal or proton uptake for the initial rate data presented in Figs. 2, 3, 5, 7, 8 A, 8 C, 9, and 10, respectively. Figs. S1, S4, and S6 contain additional data from the in vivo Co^{2+} uptake assay. Figs. S7 and S9 contain additional initial rate data at different voltages from the data presented in Fig. 8 A and 8 C, respectively. Table S1 summarizes the effects of mutagenesis data presented in Figs. 7, 8, and 9.

Results

The membrane potential accelerates DraNramp metal transport rates

Our investigation of the role of transmembrane (TM) voltage in DraNramp's mechanism stems from trying to reconcile an apparent inconsistency between in vivo and in vitro protein behavior. Purified DraNramp reconstituted into proteoliposomes (Figs. 2 A and S1) with large metal substrate gradients transported Cd^{2+}, a toxic metal known to be a good Nramp substrate (Courville et al., 2008; Illing et al., 2012), but not the biological substrates Mn^{2+} or Fe^{2+}, or similar metals such as Zn^{2+} or Co^{2+} (Figs. 2 B and S1 D). In contrast DraNramp robustly transported Co^{2+} when expressed in E. coli (Fig. S1 B).

Bacteria, including E. coli, maintain a membrane potential ($\Delta\Psi$) between –140 and –220 mV (Bot and Prodan, 2010), which greatly influences ion transport thermodynamics. When we applied voltage across proteoliposome membranes using K^+ gradients and the K^+-specific ionophore valinomycin, DraNramp transported Mn^{2+} at –40 mV or below (Fig. 2 B), and Fe^{2+}, Zn^{2+}, and Co^{2+} at –80 mV (Figs. 2 B and S1 D), with notable acceleration at –120 mV (Figs. 2 B and S1 D). Indeed, by measuring

transport rates at 10-mV increments, under these conditions we saw metal-specific apparent threshold voltages for metal transport with Mn^{2+}, followed by Zn^{2+} and Fe^{2+}, then Co^{2+} requiring progressively larger potential differences to observe metal transport, while Cd^{2+} was transported across the whole measured range (Figs. 2 C and S1 E). In fact, when extending our liposome assay to values of $\Delta\Psi > 0$, which reduces favorability of cation entry, DraNramp still transported Cd^{2+}, but not Mn^{2+}, down its concentration gradient even at +50 mV (Fig. S1, F–H). Overall, these trends are similar to the voltage dependence of mammalian Nramp2 Fe^{2+} transport observed via electrophysiology (Gunshin et al., 1997; Chen et al., 1999; Nevo and Nelson, 2004; Xu et al., 2004; Mackenzie et al., 2006, 2007; Pujol-Giménez et al., 2017) and transport assays using radioactive Fe^{2+} (Chen et al., 1999).

We next measured transport across a range of metal concentrations at a physiologically relevant $\Delta\Psi$ of –150 mV (Fig. 2 D) to determine the Michaelis–Menten constant (K_m). The K_m for substrate at –150 mV correlated with the observed threshold voltage (Fig. 2 C): Mn^{2+} and Cd^{2+} had the lowest K_m and the lowest magnitude threshold $\Delta\Psi$, Co^{2+} had the highest K_m and highest magnitude threshold $\Delta\Psi$, and Zn^{2+} and Fe^{2+} were intermediate for both. Our K_m values are consistent with in vivo Co^{2+} uptake data (Fig. S1 I) and within an order of magnitude of prior DraNramp K_d estimates of ~10 µM for Cd^{2+} and ~10–100 µM for Mn^{2+} (Bozzi et al., 2016a). These K_m values are also of similar magnitude to previously reported values for in vivo Cd^{2+} and Mn^{2+} transport by the E. coli Nramp homologue (51% identical and 72% similar to DraNramp; Kehres et al., 2000; Haemig and Brooker, 2004; Courville et al., 2008; Lan et al., 2012). The much lower K_m values (<10 µM) for Mn^{2+} and Cd^{2+} than other divalent metal substrates is consistent with trends first observed in E. coli Nramp (Kehres et al., 2000; Makui et al., 2000) but contrasts with human Nramp2 (DMT1; 26% identical and 48% similar to DraNramp), which has K_m values for Mn^{2+}, Fe^{2+}, Co^{2+}, and Cd^{2+} in the low µM range (Forbes and Gros, 2003; Illing et al., 2012). These results suggest that these bacterial homologues have higher specificity for their intended substrate, Mn^{2+}, with incidental high Cd^{2+} affinity.

Next, to recapitulate this voltage dependence trend in the context of a bacterial membrane, we varied external $[K^+]$ in our Co^{2+}-uptake assay using DraNramp-expressing E. coli. This likely perturbed the membrane potential, as E. coli maintain a significant cytosolic $[K^+]$ (Shabala et al., 2009). While we did not directly measure changes to the bacterial membrane potential induced by the added K^+, high $[K^+]$ indeed drastically decreased DraNramp Co^{2+} transport (Figs. 2 E and S1 J; see Fig. S6 below for comparison to DraNramp point mutants). As this trend was consistent with our liposome assay results (Figs. 2 C and S1 E), we suspect that the added K^+ had the intended effect of reducing the magnitude of $\Delta\Psi$.

As one explanation for our results, the membrane potential might perturb DraNramp's gross conformational landscape, with the outward-facing state relatively destabilized at lower magnitude voltages, as seen with the structurally related SGLT1 transporter (Loo et al., 1998). However, although high extracellular $[K^+]$ greatly impaired Co^{2+} transport, it had little effect
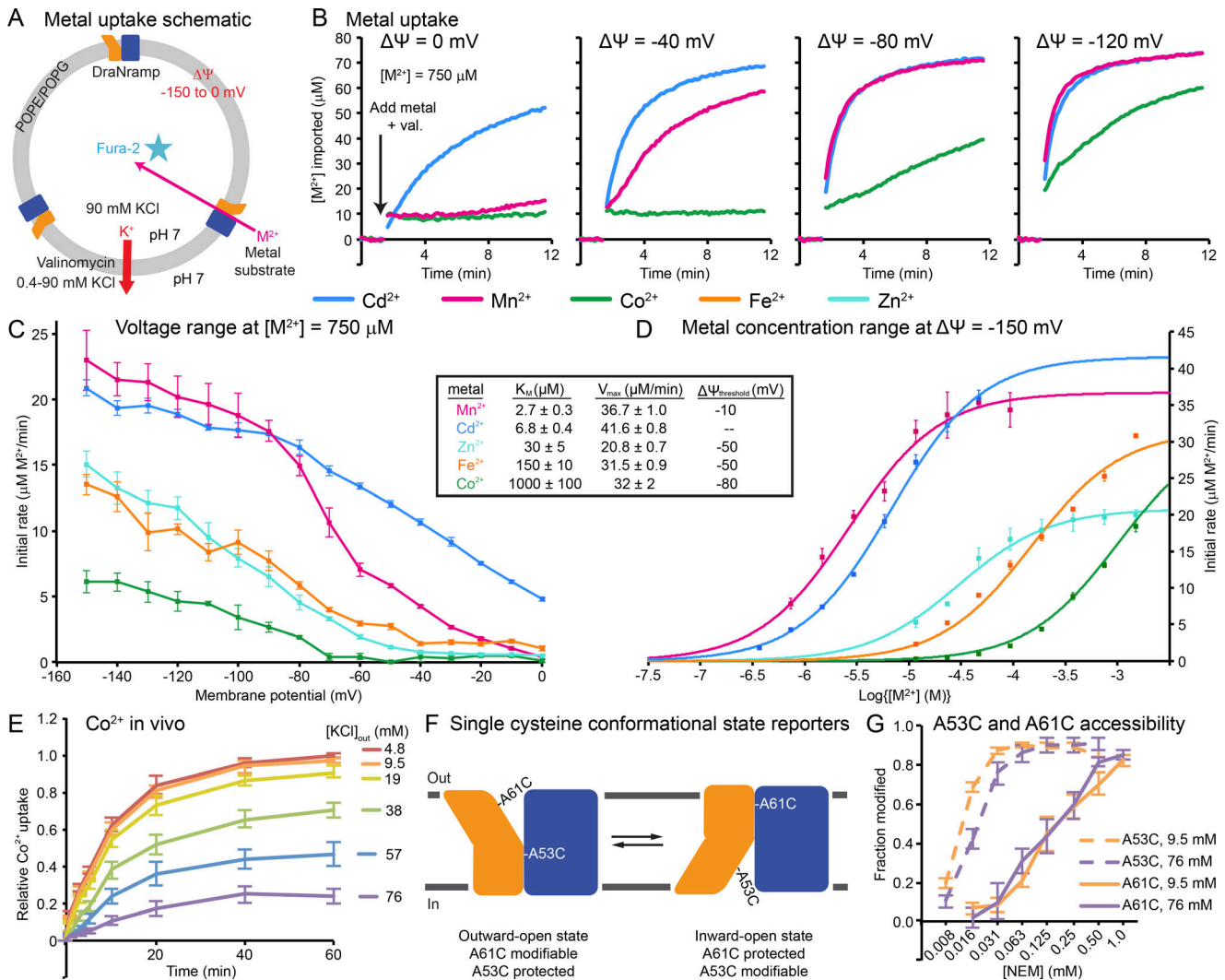
Figure 2. **Metal transport shows strong voltage dependence. (A)** Schematic of proteoliposome assay for metal transport at variable membrane potentials (ΔΨ) established by using K⁺ gradients and valinomycin. The metal-sensitive dye Fura-2 was used to detect metal uptake. No pH gradient was used in these experiments. **(B)** Representative time traces ($n = 8$) of Cd^{2+}, Mn^{2+}, and Co^{2+} transport at different ΔΨs; only Cd^{2+} is transported at ΔΨ = 0 mV. After recording a baseline, the indicated external metal concentration (750 µM for these and all subsequent traces unless otherwise indicated) and valinomycin were added, and transport was monitored for 5–10 min. **(C)** Average initial transport rate ± SEM ($n = 4$) versus membrane potential. Each metal except Cd^{2+} has a characteristic threshold negative voltage for transport to occur: –10 mV for Mn^{2+}, –50 mV for Fe^{2+} and Zn^{2+}, and –80 mV for Co^{2+}. **(D)** Average initial transport rate ± SEM ($n = 2$–3) versus metal concentration at ΔΨ = –150 mV. Comparison of C and D (table inset) shows that higher-magnitude threshold voltages correlate with K_m, indicating that voltage dependence of transport rate may be enforced through a metal-binding step. Errors in K_m and V_{max} encompass the uncertainty of fit (shown as curved lines) to data. **(E)** Time course of Co^{2+} uptake at pH 7.0 and variable [KCl] shows that high extracellular [KCl] reduces Co^{2+} uptake in *E. coli*. **(F)** Complementary single-cysteine reporters to assess conformational cycling of DraNramp. **(G)** Fraction of modified cysteine versus NEM concentration at pH 7. Inward (A53C) and outward (A61C) reporters were both labeled, even at high [KCl]$_{out}$ that depresses Co^{2+} uptake. Conformational locking thus cannot explain reduced Co^{2+} transport by DraNramp under these conditions. Data in E and G are averages ± SEM ($n = 4$). See also Fig. S1.

on the accessibility to NEM modification of single-cysteine reporters that are exposed to bulk solvent either only in the inward-open (A53C) or outward-open (A61C) states (Bozzi et al., 2016b, 2019; Fig. 2, F and G; and Fig. S1 K). This suggests that the membrane potential does not cause gross changes in the DraNramp conformational preference, although more sophisticated measurements could still uncover effects of TM voltage on conformational landscape. This finding is, however, consistent with the observed substrate-specific threshold voltages, as a shift in conformational equilibrium that completely inhibits transport of all metals (as seen with conformationally locked

DraNramp variants; Bozzi et al., 2016b, 2019) does not account for these differences. Our consistent in vivo and in vitro findings indicate that the reconstituted transporter does indeed function the same as in the native membrane, and that TM voltage, which was not controlled for in our initial reconstitutions, is a critical variable controlling metal transport kinetics.

Acidic outside pH gradients accelerate DraNramp metal import
In addition to ΔΨ's importance, for a wide range of Nramp homologues, low external pH accelerates metal transport (Gunshin et al., 1997; Agranoff et al., 1999, 2005; Chen et al., 1999; Kehres
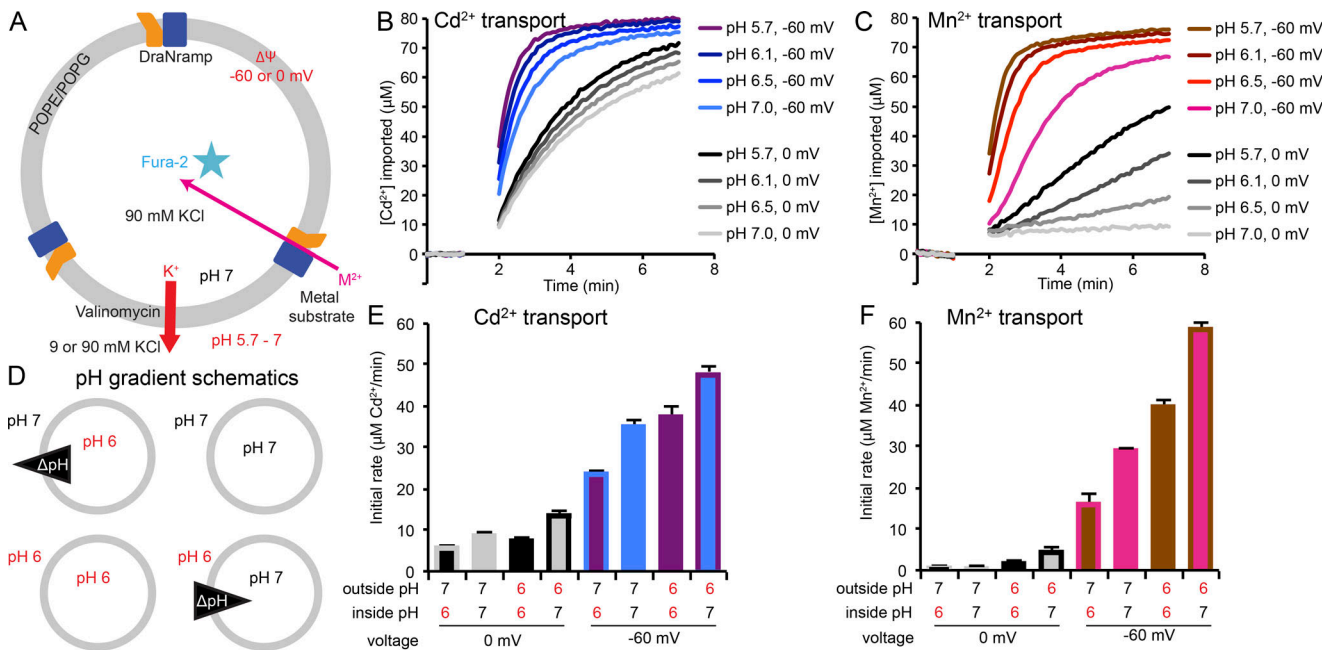
Figure 3. **Acidic external pH and favorable outside-to-inside pH gradients stimulate metal transport. (A)** Schematic for assessing effect of varying external pH on metal transport in proteoliposomes with internal pH 7. K^+ gradients and valinomycin were used to set $\Delta\Psi = 0$ or -60 mV. A strong external buffer was added to adjust the pH to the indicated value when metal and valinomycin were added after the baseline read. **(B and C)** Representative time traces ($n \geq 4$) of 750 µM Cd^{2+} (B) or Mn^{2+} (C) uptake into proteoliposomes. Acidic-outside ΔpH accelerated Cd^{2+} and Mn^{2+} transport (at $\Delta\Psi = -60$ mV) and enabled Mn^{2+} uptake when $\Delta\Psi = 0$. **(D)** Schematic for discriminating between effect of low pH and ΔpH on metal transport rate by varying internal and external pH. **(E and F)** Initial metal uptake rates show that Cd^{2+} uptake (E) was accelerated by a favorable ΔpH, while Mn^{2+} uptake (F) was faster in the presence of lower external pH and further accelerated by a favorable ΔpH. Data are averages ± SEM ($n \geq 3$). See also Fig. S2.

et al., 2000; Makui et al., 2000; Tandy et al., 2000; Sacher et al., 2001; Buracco et al., 2015). We therefore compared DraNramp Cd^{2+} and Mn^{2+} transport in proteoliposomes in the presence of an acidic outside pH gradient (ΔpH) of varying magnitudes (Fig. 3 A). While ΔpH moderately enhanced Cd^{2+} transport (Fig. 3 B), it more dramatically accelerated Mn^{2+} transport, even enabling transport at 0 mV (Fig. 3 C).

The observed stimulation could result from lower pH, a favorable ΔpH, or a combination of both factors increasing DraNramp's metal transport rate. We therefore reconstituted DraNramp into proteoliposomes with internal pH of 6 or 7 and measured Cd^{2+} and Mn^{2+} transport in the presence and absence of a ΔpH at either $\Delta\Psi = 0$ or -60 mV (Fig. 3 D). For Cd^{2+} and Mn^{2+}, a favorable ΔpH (6 outside and 7 inside) accelerated transport compared with no ΔpH, while unfavorable ΔpH (7 outside and 6 inside) slowed uptake (Fig. 3, E and F), with Mn^{2+} again showing a wider spread of transport rates (Fig. S2). With no ΔpH, Cd^{2+} transport rates were similar at acidic pH (6 outside and inside) or neutral pH (7 outside and inside; Figs. 3 E and S2 A). In contrast, in the absence of ΔpH, acidic pH somewhat accelerated Mn^{2+} transport compared with neutral pH (Figs. 3 F and S2 B). Overall, low pH and ΔpH had larger-magnitude effects on Mn^{2+} transport rates than on Cd^{2+} transport rates.

Voltage and pH gradients affect K_m and V_{max} of DraNramp metal transport
To further investigate the effects of TM voltage and pH gradients on DraNramp transport, we determined Michaelis–Menten

parameters for Mn^{2+} and Cd^{2+} transport kinetics in the absence or presence of a favorable ΔpH at three $\Delta\Psi$ values (Fig. 4). For both metals, with and without ΔpH, a more negative $\Delta\Psi$ increased transport efficiency by improving both K_m and V_{max}. Strikingly, in the absence of ΔpH, hyperpolarizing $\Delta\Psi$ from -50 to -150 mV decreased the K_m values for Cd^{2+} and Mn^{2+} >20- and 300-fold, respectively. Thus, in addition to its potential to act as a thermodynamic driving force, $\Delta\Psi$ appears to shape the free energy landscape that dictates DraNramp transport kinetics and may therefore influence metal binding and other steps in the transport mechanism. While in all six cases ΔpH increased V_{max}, the effects on K_m were mixed (Fig. 4). Indeed, ΔpH decreased K_m for both metals at lower-magnitude $\Delta\Psi$ but increased K_m at higher-magnitude $\Delta\Psi$. Generally, $\Delta\Psi$ and ΔpH are more synergistic for Mn^{2+} and more antagonistic for Cd^{2+}, which may hint at a mechanistic difference for how DraNramp transports these two metal substrates.

Stimulation of proton transport is substrate specific in DraNramp
Like other Nramp homologues (Gunshin et al., 1997; Chen et al., 1999; Mackenzie et al., 2007; Ehrnstorfer et al., 2017), DraNramp also transports protons in addition to divalent metals (Bozzi et al., 2019). We therefore measured H^+ transport by DraNramp (Fig. 5 A) at a range of voltages in the absence or presence of metal substrate (Figs. 5 B and S3 A). While DraNramp efficiently transported all tested metals (except Ca^{2+}) at -120 mV and to some degree at -80 mV (Figs. 2 B and S1 D), only Mn^{2+},
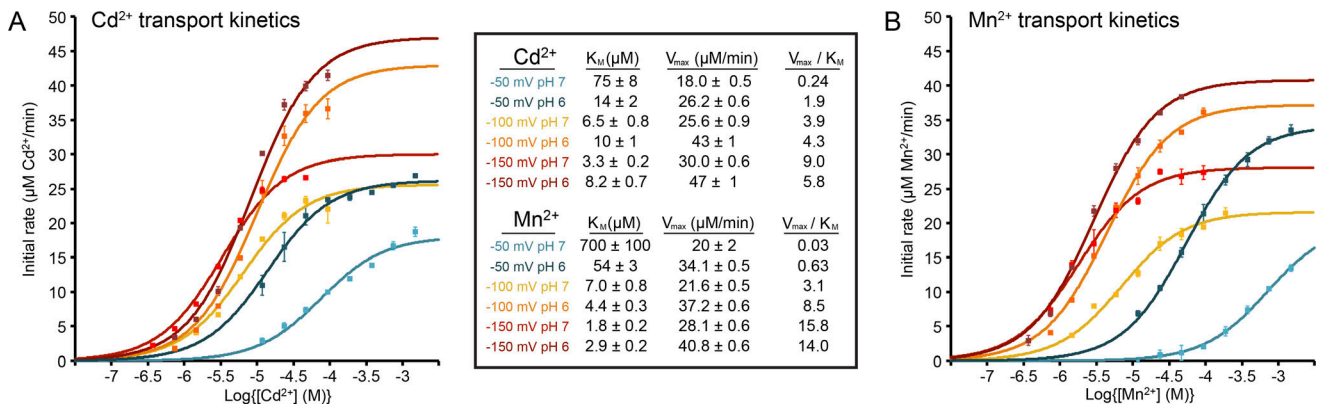
Bozzi et al.
Nramp M^{2+}:H^+ cotransport and uniport mechanisms

Journal of General Physiology
https://doi.org/10.1085/jgp.201912428

1418

Figure 4. **Voltage and pH gradients govern metal transport kinetics. (A and B)** Dose–response curves for Cd^{2+} (A) and Mn^{2+} (B) transport at different external pH and $\Delta\Psi$ values in proteoliposomes with internal pH = 7. Data are averages ± SEM (n = 3). Errors in K_m and V_{max} reported in the inset table encompass the uncertainty of the fit (shown as curved lines) to the data.

Fe^{2+}, and Co^{2+} stimulated H^+ influx above basal rates (Fig. 5 C). Despite robust Cd^{2+} uptake across all potentials, Cd^{2+} failed to stimulate significant H^+ transport. Indeed, at –120 mV, where H^+ uniport (uptake in the absence of added metal) became significant, Cd^{2+} noticeably reduced the H^+ influx rate (Fig. 5, B and C). DraNramp's two best substrates, which should nearly saturate the metal-binding site at –80 and –120 mV, gave initial rate stoichiometries of ~1 H^+:1 Mn^{2+} and 0 H^+: 1 Cd^{2+} (Fig. 5 C), confirming that proton-metal cotransport is substrate specific.

In addition, across a range of Mn^{2+} concentrations, higher Mn^{2+}-transport rates corresponded with higher H^+-transport rates (Fig. S3, B and C), consistent with the trend previously seen for *Eremococcus coleocola* Nramp in proteoliposomes (Ehrnstorfer

et al., 2017). Interestingly, H^+:Fe^{2+} stoichiometries significantly exceeded the 1:1 seen for Mn^{2+}, which may reflect an additional complexity in the DraNramp transport mechanism that we do not yet fully understand; indeed, highly variable, condition-dependent H^+:Fe^{2+} stoichiometries were previously reported for eukaryotic Nramp homologues (Chen et al., 1999).

Taken together with the fact that ΔpH affected the transport kinetics of both Mn^{2+} and Cd^{2+}, this indicates that "proton-metal coupling" in Nramps comprises at least two distinct phenomena: (a) ΔpH accelerates metal transport and (b) H^+ cotransport is stimulated by certain metal substrates. Below, using insights gleaned from DraNramp's structures and mutagenesis experiments, we begin to mechanistically explain these surprising results.
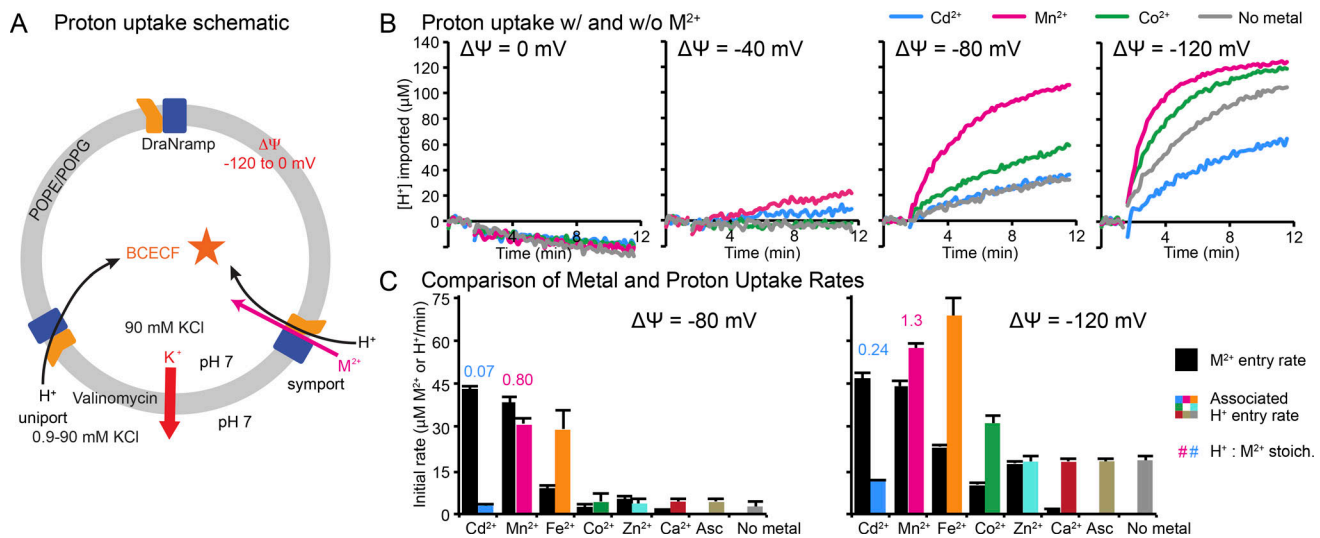

Figure 5. **Proton cotransport is metal specific. (A)** Schematic for detecting H^+ influx into proteoliposomes at various $\Delta\Psi$ values, pH 7.0 on both sides, in the absence or presence of 750 µM metal substrate. The setup was identical to that used in Fig. 2 (A and B), except the pH-sensitive dye BCECF replaced the metal-sensitive dye Fura-2. **(B)** Representative time traces (n = 8) of H^+ uptake into proteoliposomes. Negative $\Delta\Psi$ drove DraNramp H^+ import. Mn^{2+} and Co^{2+} stimulated H^+ entry, while Cd^{2+} did not and instead reduced H^+ influx at $\Delta\Psi$ = –120 mV. **(C)** Initial metal (black) and H^+ (color) uptake rates show that Mn^{2+}, Fe^{2+}, and Co^{2+} transport stimulated H^+ influx above its basal no-metal rate, while Cd^{2+} and Zn^{2+} transport did not. Stoichiometry ratios (numbers above bars) were calculated for Cd^{2+} and Mn^{2+} and were ~1:1 for Mn^{2+}:H^+ transport in the presence of metal. Data are averages ± SEM (n ≥ 4). See also Fig. S3.
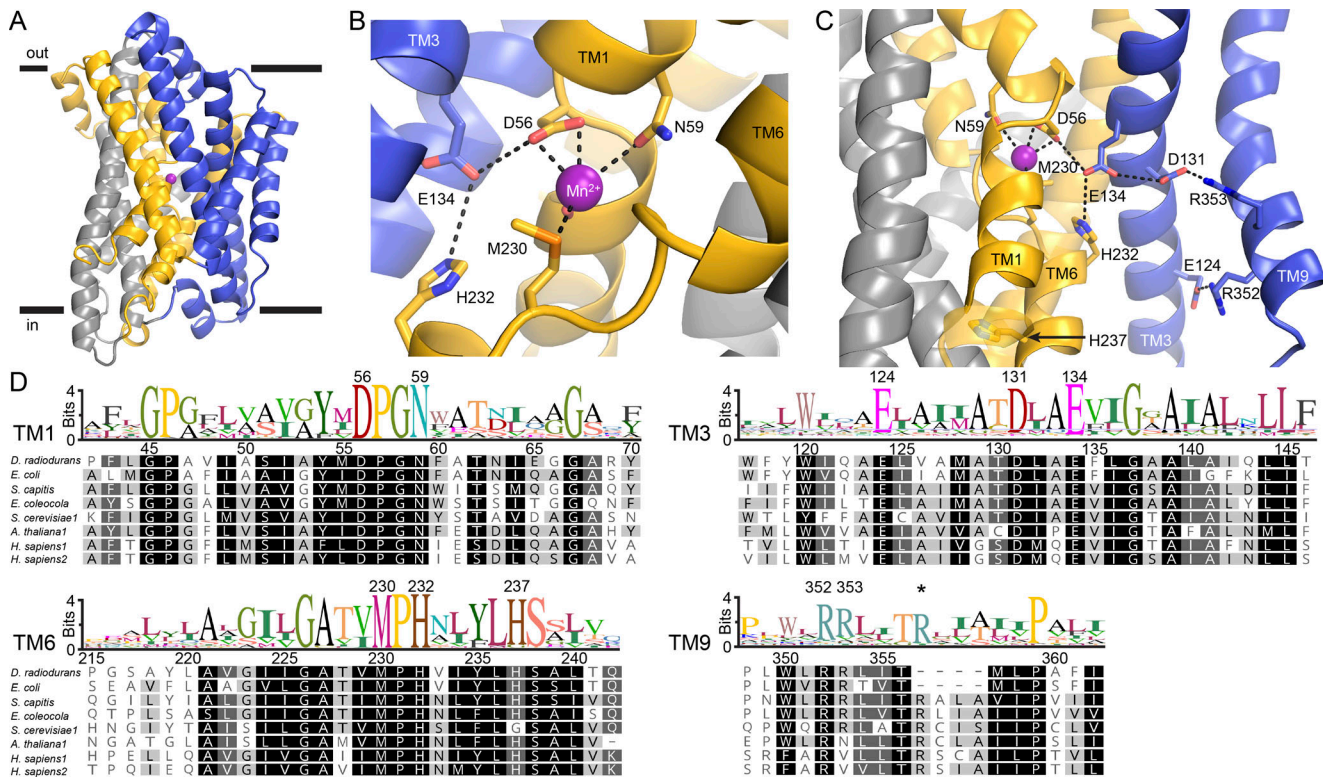
Figure 6. **A network of highly conserved charged and protonatable residues adjoins the metal-binding site. (A)** Crystal structure of DraNramp in an outward-open conformation bound to Mn^{2+} (magenta sphere; PDB accession no. 6BU5; Bozzi et al., 2019). TMs 1, 5, 6, and 10 are gold; TMs 2, 7, and 11 are gray; and TMs 3, 4, 8, and 9 are blue. **(B)** D56, N59, M230, and the A53 carbonyl coordinate Mn^{2+} in the outward-open state, along with two waters (not depicted). **(C)** View from the plane of the membrane of a network consisting of E134, H232, D131, R353, R352, and E124 that extends ~20 Å from D56 to the cytosol. TMs 8 and 4–5, in front of TMs 3 and 9, respectively, were removed for clarity. **(D)** Sequence logos from an alignment of 6,878 Nramp sequences. All 10 mutated residues (numbers above) are highly conserved. Canonical helix-breaking motifs at the metal-binding site are DPGN in TM1 and MPH in TM6. TM6's H237 is a glycine in many fungal homologues. The second TM9 arginine (R353) varies in location (*) due to an extra helical turn in many homologues; this insertion contains a third arginine in some homologues. See also Fig. S4.

DraNramp metal-binding site abuts an extended salt-bridge network

Our structures of DraNramp in multiple conformational states (Bozzi et al., 2016b, 2019) provide a framework to understand the mechanistic details of voltage dependence, ΔpH stimulation, and metal-stimulated proton transport. DraNramp's 11 α-helical TM segments adopt the common LeuT-fold (Yamashita et al., 2005; Boudker and Verdon, 2010; Forrest et al., 2011; Shi, 2013; Fig. 6 A). Conserved residues D56, N59, and M230 coordinate metal substrate throughout the transport process (Ehrnstorfer et al., 2014; Bozzi et al., 2019; Fig. 6 B). Below the binding site, conserved H237 on TM6b lines the metal's exit route to the cytosol (Bozzi et al., 2019; Figs. 6 C and S4 A). Adjacent to D56, a conserved network of charged and protonatable residues leads into the structurally rigid cluster formed by TMs 3, 4, 8, and 9 to provide a parallel ~20-Å H^+-transport pathway toward the cytosol (Bozzi et al., 2019; Fig. 6, C and D; and Fig. S4, A and B). These residues form a sequence of three interacting pairs: H232-E134, D131-R353, and R352-E124. This salt-bridge network is unique to the Nramp clade in the LeuT family of structurally and evolutionarily related transporters (Cellier, 2012, 2016; Bozzi et al., 2019).

In multiple Nramp homologues, D56 and N59 contribute to metal transport (Courville et al., 2008; Ehrnstorfer et al., 2014, 2017; Bozzi et al., 2016a, 2019), while M230 contributes to a selectivity filter that favors transition metals over alkaline earth metals (Ehrnstorfer et al., 2014; Bozzi et al., 2016a). Mutations to E124, D131, E134, H232, and H237 abrogate Mn^{2+} transport in *E. coli* Nramp (Haemig and Brooker, 2004; Haemig et al., 2010), while mutations to H232 and H237 (Lam-Yuk-Tseung et al., 2003; Mackenzie et al., 2006) and R353 (Lam-Yuk-Tseung et al., 2006) impair metal transport in mammalian DMT1, with the latter mutation also causing anemia (Iolascon et al., 2006). Recent studies using different Nramp homologues implicated E134 or H232 in proton–metal coupling (Ehrnstorfer et al., 2017; Pujol-Giménez et al., 2017), and we demonstrated the importance of D56 and D131 in addition to E134 and H232 to DraNramp H^+ transport (Bozzi et al., 2019). From structure-based pK_a predictions, we therefore proposed D56 as the initial proton-binding site and D131 as the subsequent proton acceptor required for TM transport (Bozzi et al., 2019).

Hypothesizing that this network of conserved charged and protonatable residues contributes to the voltage dependence and proton–metal cotransport phenomena, we designed a panel of point mutations that remove or neutralize these sidechains via
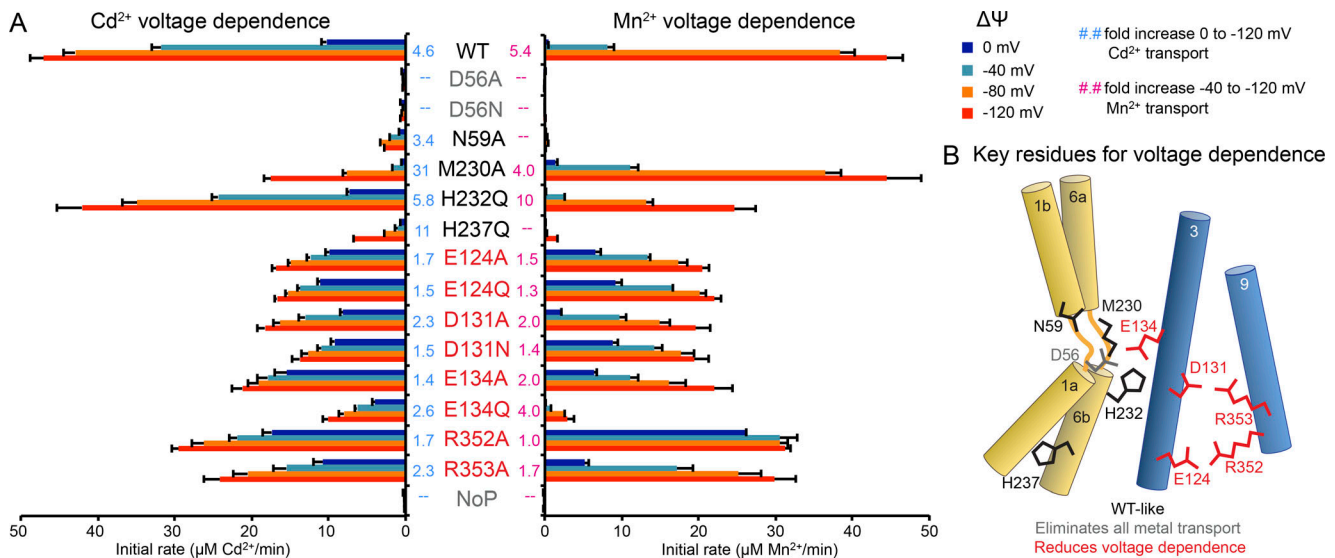
Bozzi et al.
Nramp M^{2+}:H^+ cotransport and uniport mechanisms

Journal of General Physiology   1420
https://doi.org/10.1085/jgp.201912428

Figure 7. **Mutations to the conserved salt-bridge network perturb voltage dependence of metal transport rate. (A)** Average initial metal uptake rates ± SEM ($n \geq 4$) for DraNramp mutants at different $\Delta\Psi$ (0 to –120 mV, colored bars). [M^{2+}] was 750 µM, and the pH was 7 on both sides of the membrane. The fold increase in transport rate is indicated (cyan, 0 to –120 mV for Cd^{2+}; pink, –40 to –120 mV for Mn^{2+}). Mutations to E124, D131, E134, R352, and R353 (red) reduced the $\Delta\Psi$ dependence of Cd^{2+} and Mn^{2+} transport rates across the range of tested voltages, such that they exceeded WT at low-magnitude $\Delta\Psi$ but lagged WT at physiological large-magnitude $\Delta\Psi$. Mutations to N59, M230, H232, and H237 (black) retained WT-like $\Delta\Psi$ dependence, and D56 mutants (gray) eliminated all metal transport. **(B)** Network schematic illustrates clustering of residues most important for $\Delta\Psi$ dependence (red). See also Fig. S5 for representative time traces of these results and Fig. S6 for dependence of in vivo Co^{2+} uptake rates on external [K^+].

alanine, asparagine, or glutamine substitution. All DraNramp mutants expressed well in *E. coli* (Fig. S4, C and D) and were readily purified. We reconstituted each in proteoliposomes to further explore how each conserved residue contributes to DraNramp's metal and proton transport behavior.

Mutations to conserved salt-bridge network perturb voltage dependence of metal transport rate

With our mutant panel, we first measured the effect of $\Delta\Psi$ on in vitro Cd^{2+} and Mn^{2+} transport (Figs. 7 A and S5). Most mutants retained some transport of either or both substrates, except metal-binding D56 mutants. Compared with WT, the remaining mutants clustered in two groups in terms of the impact of $\Delta\Psi$ on metal transport rate.

Mutations to N59, M230, H232, and H237 largely preserved WT-like voltage dependence. These TM1 and TM6 residues clustered in the metal-binding site or metal-release pathway (Fig. 7 B). Mutations to TM3 and TM9 salt-bridge network residues E124, R352, R353, D131, and E134 reduced voltage dependence of Mn^{2+} and Cd^{2+} transport across the tested $\Delta\Psi$s (Fig. 7). All reduced transport rates at –120 mV, but many equaled and several outperformed WT at lower-magnitude $\Delta\Psi$. Perturbing this network of residues thus alters $\Delta\Psi$'s effects on DraNramp's metal transport kinetics, such that these mutants, while moderately impaired compared with WT under physiological conditions, no longer face WT's transport restriction in the absence of $\Delta\Psi$.

We saw similar trends with this panel in vivo: salt-bridge network mutations reduced the effect of high external [K^+] on Co^{2+} transport in *E. coli* (Fig. S6), most strikingly with E134A and R352A. Overall, these results further implicate the intact salt-bridge network as contributing to the strong voltage dependence of DraNramp transport kinetics, thus eliminating most metal transport when $\Delta\Psi$ is zero or positive.

Mutations adjacent to metal-binding site eliminate ΔpH stimulation of metal transport rate

We sought to identify which residues contribute most to the observed ΔpH stimulation of DraNramp metal transport (Fig. 3). We therefore measured Mn^{2+} transport by our mutants in liposomes across a range of external pHs (and thus ΔpHs) in either the absence or presence of a $\Delta\Psi < 0$ (Figs. 8 A and S7). Mutant phenotypes again clustered in three groups (Fig. 8 B). As before, mutants to metal-binding D56 and N59 eliminated Mn^{2+} transport, while H237Q showed slight activity in the presence of both $\Delta\Psi$ and ΔpH. As with voltage dependence, all mutants to the E124-R352-R353-D131-E134 network reduced the Mn^{2+}-transport enhancement provided by ΔpH to a level comparable to Cd^{2+} in WT. Strikingly, mutants M230A, H232Q, and E134Q, all near metal-binding D56, eliminated ΔpH stimulation, such that unlike WT, Mn^{2+} transport was not observed in the absence of $\Delta\Psi$, no matter the ΔpH (Fig. S7). Thus, the immediate vicinity of the metal-binding site is most crucial for the kinetic stimulation provided by ΔpH, while more distant salt-bridge network residues contribute to a lesser degree.

Mutations throughout the salt-bridge network alter proton transport behavior

We previously showed that mutations to D56, H232, E134, and D131 eliminated DraNramp's voltage-driven proton uniport, thus leading us to propose those four residues as the core of a conserved proton-transport pathway (Bozzi et al., 2019). In
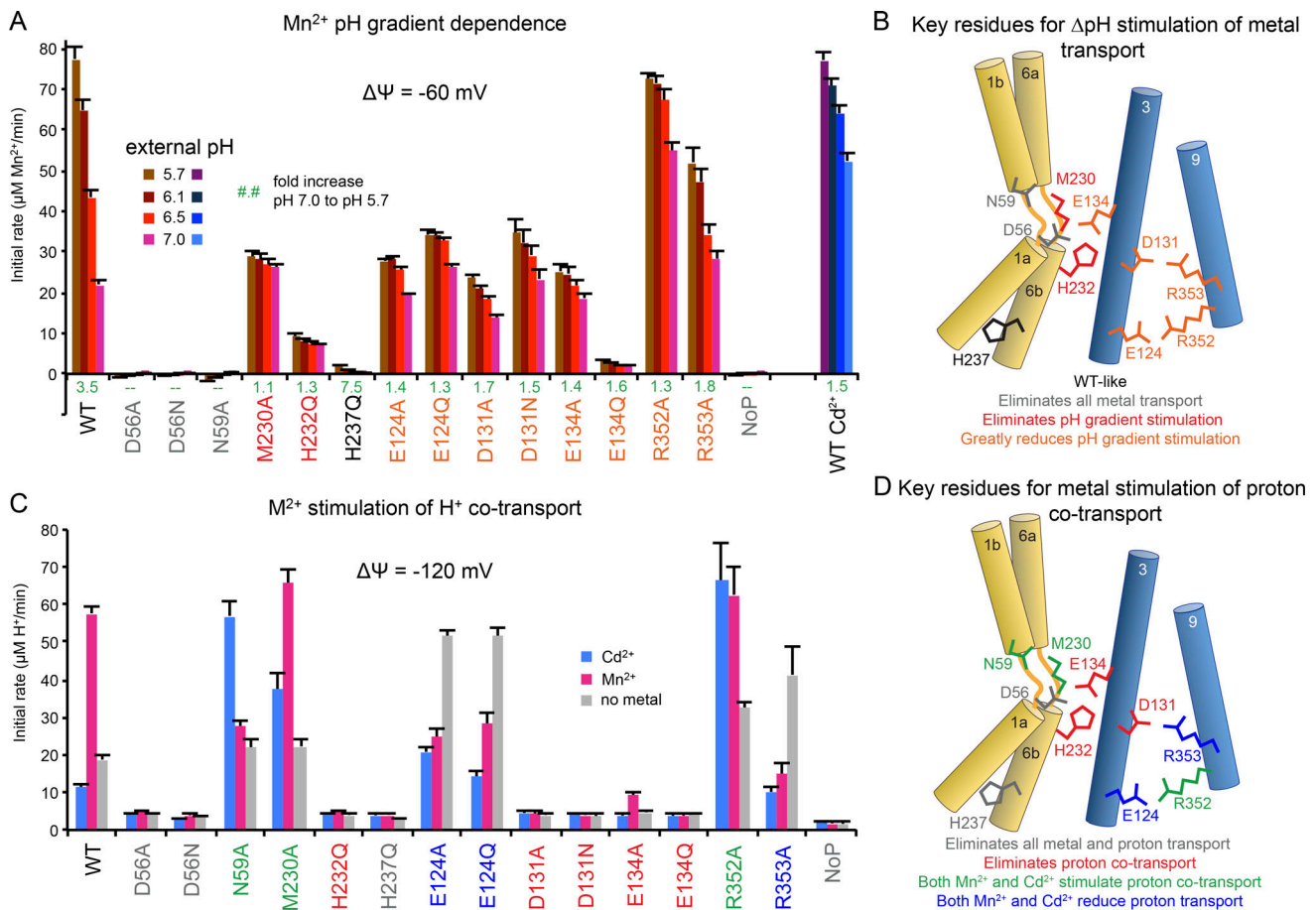
Figure 8. **Mutations to conserved network reduce or eliminate ΔpH stimulation of Mn²⁺ transport and perturb or eliminate H⁺ cotransport.** **(A)** Average initial Mn²⁺ uptake rates ± SEM ($n \geq 4$) in proteoliposomes at various external pHs, internal pH = 7, and ΔΨ = −60 mV, as in Fig. 3 (A–C). [Mn²⁺] was 750 μM. **(B)** Schematic shows proximity to binding site of residues where mutations fully eliminate the ΔpH stimulation effect (red), while more distant mutations within the salt-bridge network still decrease the ΔpH effect (orange). See also Fig. S7 for representative time traces of these results. **(C)** Average initial metal-stimulated H⁺ transport rates ± SEM ($n \geq 4$) at ΔΨ = −120 mV with pH 7.0 on both sides of the membrane, in the absence or presence of 750 μM M²⁺ as in Fig. 5. **(D)** Schematic shows that protonatable residues in immediate vicinity of D56 are essential for metal-stimulated H⁺ transport, while the entire network affects proton-metal cotransport behavior. Interestingly, D131 and E134 mutants retain some ΔpH stimulation while eliminating metal-stimulated H⁺ cotransport, while M230A shows the opposite pattern. Mutations to the salt-bridge network residues furthest from D56 increase rate of H⁺ transport without metal but have variable effects on metal stimulation. See also Fig. S8 for representative time traces of these results and Fig. S9.

addition, mutations to the more-distant salt-bridge network residues R353, R352, and E124 increased the rate of proton uniport (Bozzi et al., 2019). Here we measured how metal substrates Cd²⁺ and Mn²⁺ affect proton transport at −120 and −80 mV for our mutant panel (Figs. 8 C, S8, and S9). Mutations to D56, H232, E134, and D131 eliminated metal-stimulated H⁺ transport (although E134A retained slight Mn²⁺ stimulation). Thus, the same four residues that are indispensable for proton uniport are also required for metal-evoked proton uptake, suggesting that uniported and cotransported protons follow the same pathway. (While H237Q also eliminated basal and metal-stimulated H⁺ transport, this phenotype most likely arises from that mutation preventing the protein from sampling the outward-open state needed for proton transport to occur; Bozzi et al., 2019). In contrast to its inhibition of WT, Cd²⁺ stimulated H⁺ uptake for mutants to metal-binding N59 and M230, and R352 18 Å away (Figs. 8 C, S8, and S9). Strikingly, for the E124 and R353 mutants, either Mn²⁺ or Cd²⁺ sharply reduced H⁺

transport (Figs. 8 C, S8, and S9); thus Mn²⁺ now behaved more like Cd²⁺ did for WT.

Overall, any mutation to the extended network eliminated the distinction between Cd²⁺ and Mn²⁺ in terms of proton cotransport (Fig. 8 D). This is consistent with previous observations of subtle perturbations to this network affecting proton transport in other Nramp homologues, as seen with an anemia-causing mutation G185R on TM4 in mouse Nramp2 (Fleming et al., 1998; Su et al., 1998; G153R in DraNramp) directly above the R353-D131 pair (Xu et al., 2004), and an F-to-I substitution in human Nramp2 at the DraNramp equivalent L164 adjacent to R352-E124 (Nevo and Nelson, 2004). Curiously, some DraNramp mutants (D131A, E134A) retained some ΔpH (and/or low pH) stimulation of Mn²⁺ transport but little Mn²⁺ stimulation of H⁺ transport, while others (M230A, R352A) had the opposite effect, with little ΔpH (and/or low pH) stimulation but robust Mn²⁺ stimulation. In contrast, H232Q eliminated both effects, consistent with the H-to-A mutant in *E. coleocola* Nramp
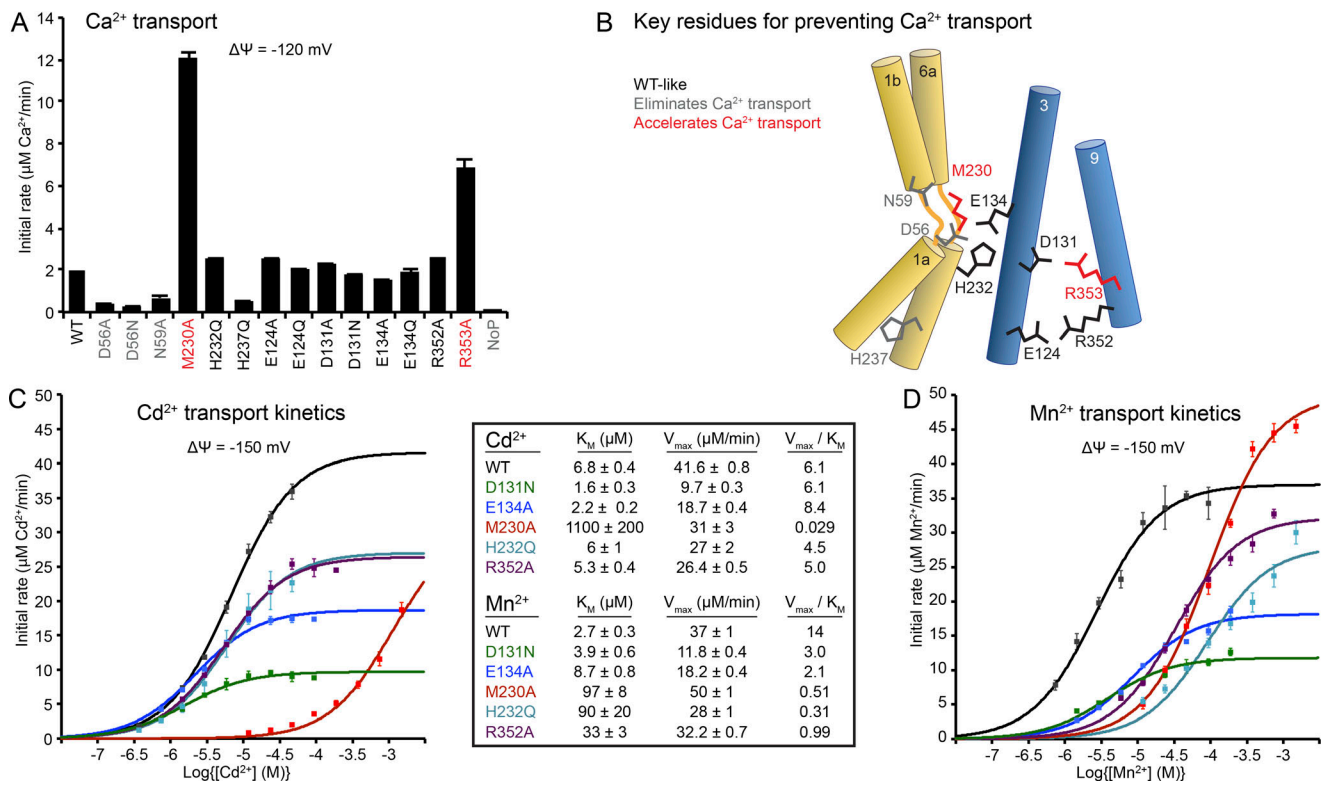
Figure 9. **Perturbations to the conserved salt-bridge network alter metal selectivity and increase K_m for Mn^{2+}. (A)** Average initial Ca^{2+} transport rates ± SEM ($n \geq 4$) at −120 mV with pH 7.0 on both sides of the membrane and 750 µM Ca^{2+}. **(B)** Schematic of mutation locations. M230A, or R353A, 15 Å away; both increased Ca^{2+} transport. D56 and N59 mutations eliminated Ca^{2+} uptake, and other mutants were similar to WT. **(C and D)** Dose–response curves of Cd^{2+} (C) or Mn^{2+} (D) transport at −150 mV with pH 7.0 on both sides of the membrane for a subset of mutants that reduce or eliminate $\Delta\Psi$ dependence, ΔpH stimulation, or metal-dependent proton transport. Data are averages ± SEM ($n \geq 2$). The resulting transport kinetic values (middle) show significant overlap for Cd^{2+} transport but wider separation for the physiological substrate Mn^{2+}. M230A is the only mutation that impaired Cd^{2+} transport more severely than Mn^{2+} transport. Errors in K_m and V_{max} encompass the uncertainty of the fit to the data. See also Fig. S10 for representative time traces of the data in A.

(Ehrnstorfer et al., 2017), while D56 mutations eliminated all metal and proton transport. These mutagenesis results further suggest that ΔpH stimulation of metal transport rate need not necessarily arise from a proton cotransport requirement.

Perturbing the salt-bridge network alters K_m and selectivity
As high transport efficiency requires selectivity against potential competing substrates, we tested whether our mutants transport Ca^{2+}, an abundant alkaline earth metal that Nramps must discriminate against (Fig. 9, A and B; and Fig. S10). Most mutations did not increase Ca^{2+} transport. Thus, their perturbations of voltage and ΔpH dependence of metal transport rate do not arise from indiscriminate metal transport. Metal-binding D56 and N59 mutants reduced Ca^{2+} transport below WT levels, indicating that Ca^{2+} transport requires the same metal-binding site as other metals. Two mutations enhanced Ca^{2+} uptake: M230A, which removes the metal-coordinating methionine that preferentially stabilizes transition metals (Bozzi et al., 2016a), and R353A. The altered selectivity of R353A, 15 Å from the bound metal, is reminiscent of G153R, which adds exogenous positive charge to the salt-bridge network region and, despite not being part of the primary coordination sphere, can structurally perturb the metal-binding site to improve Ca^{2+} transport (Xu et al., 2004; Bozzi et al., 2016b).

We next compared Cd^{2+} and Mn^{2+} transport by select mutants across a range of metal concentrations to understand how these residues impact transport under more physiologically relevant conditions (Fig. 9, C and D). Most mutations had little impact on Cd^{2+} transport even at low µM concentrations and thus retained transport efficiency (calculated as V_{max}/K_m) within twofold of WT. The exception was M230A, which drastically reduced Cd^{2+} transport, consistent with the importance of this residue for Cd^{2+} affinity (Ehrnstorfer et al., 2014; Bozzi et al., 2016a, 2019). In contrast, all mutations reduced Mn^{2+} transport rate at environmentally relevant low Mn^{2+} concentrations, resulting in 5- to 50-fold lower efficiency. Thus, mutagenic perturbations to the transporter that reduce voltage dependence or eliminate the metal-stimulated proton transport also impair function under physiological conditions. That these mutations alter DraNramp's relative substrate preferences is consistent with an allosteric functional link between the salt-bridge network and the metal-binding site.

Mutations to the salt-bridge network increase deleterious Mn^{2+} back-transport
Finally, we probed whether mutations to the salt-bridge network that perturbed voltage dependence and proton transport may also impact the observed directional bias of DraNramp
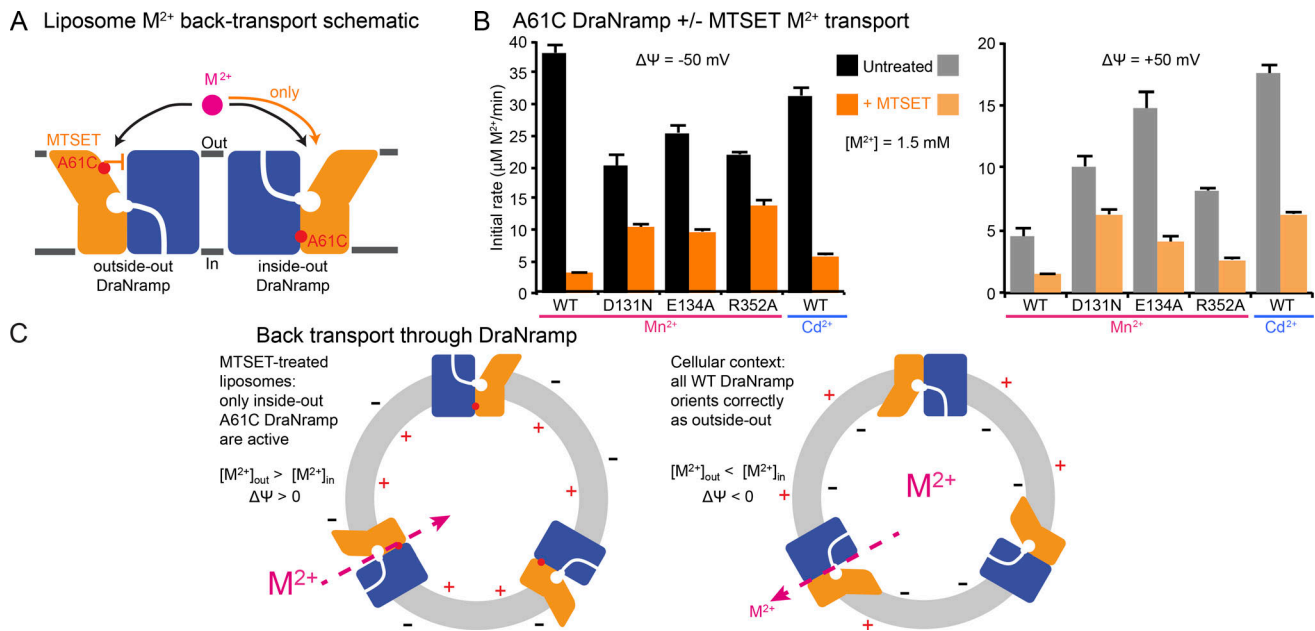
Figure 10. **Mutations to the salt-bridge network enable deleterious Mn²⁺ back transport. (A)** Schematic for isolating metal-transport activity from the ~50% inside-out transporters (Bozzi et al., 2019). Only outside-out transporters are incapacitated by A61C modification with MTSET. **(B)** Average initial transport rates ± SEM (n = 4) of MTSET-treated or untreated proteoliposomes at $\Delta\Psi$ = −50 mV (left) or +50 mV (right; note that the axis scales are different). pH = 7 on both sides of the membrane, and [M²⁺] = 1.5 mM. MTSET essentially eliminated WT-like's Mn²⁺ transport. In contrast, D131N, E134A, and R352A retained significant Mn²⁺ transport, likely reflecting increased activity from inside-out transporters. In addition, MTSET treatment eliminated more Mn²⁺ transport than Cd²⁺ transport, which did not require H⁺ cotransport (Fig. 5). **(C)** A61C liposome assay mimics cellular context for DraNramp back transport. Metal influx into MTSET-treated proteoliposomes occurs down a concentration gradient but against a $\Delta\Psi > 0$, just as metal efflux would in vivo. See also Fig. S11 for representative time traces of these results.

metal transport (Bozzi et al., 2019). We reconstituted DraNramp constructs containing the C382S mutation to remove the lone endogenous cysteine and the single-cysteine A61C that lines the external vestibule (Bozzi et al., 2016b) and applied membrane-impermeable MTSET. Covalent modification of A61C with MTSET nearly eliminates metal transport in vivo (Bozzi et al., 2016b) and in vitro (Bozzi et al., 2019), likely by preventing outward-to-inward conformational change essential for metal transport (Bozzi et al., 2019; Fig. S11 B). DraNramp orients randomly in proteoliposomes with ~50% inside-out and ~50% outside-out (Bozzi et al., 2019). In proteoliposomes, MTSET treatment should incapacitate outside-out transporters, leaving inside-out proteins unaffected, and therefore theoretically capable of metal transport (Figs. 10 A and S11 A). Strikingly, while MTSET essentially eliminated Mn²⁺ transport for the WT-like protein, the salt-bridge network mutants D131N, E134A, and R352A retained significant activity at both positive and negative $\Delta\Psi$ (Figs. 10 B and S11 C). These inside-out mutant transporters shuttled Mn²⁺ down a concentration gradient against $\Delta\Psi$, which by analogy approximates back-transport in a cellular context (Fig. 10 C), while this process was only minimally observed for the WT-like protein (which, unlike the true WT, displayed slight Mn²⁺ transport at $\Delta\Psi \geq 0$). Thus, these point mutations, which all reduced the voltage and ΔpH dependence of metal transport (Figs. 7 and 8), also weakened DraNramp's kinetic bias favoring outside-to-inside metal transport. Notably, MTSET-treated WT-like protein transported more Cd²⁺ than Mn²⁺ (Figs. 10 B and S11 C). Because Cd²⁺, unlike Mn²⁺, does not stimulate H⁺ uptake

(Fig. 5), this suggests that DraNramp's proton cotransport requirement is important to bias the transporter toward inward metal transport. Altogether, disruption of voltage dependence and proton–metal cotransport, through either mutagenesis or by metal identity, likely promotes metal efflux under physiological conditions.

Discussion

Our kinetic studies with DraNramp show that a range of transport processes can occur under physiological conditions (Fig. 11 A). Metal and proton transport rate measurements reveal DraNramp performs H⁺ uniport, 1:1 Mn²⁺:H⁺ cotransport, and Cd²⁺ uniport (Fig. 5). Thus, the expected kinetic barriers that would prevent uncoupled transport in canonical symporters must be significantly diminished in DraNramp (Fig. 11 B). However, we do not observe Mn²⁺ uptake by WT DraNramp without accompanying H⁺, suggesting that efficient Mn²⁺ transport may require the presence of a H⁺ cosubstrate. Furthermore, membrane potential dramatically affects the rates of all DraNramp transport events, to the extent that a sufficiently negative $\Delta\Psi$ is required for otherwise thermodynamically favorable metal transport to occur on the time-scale of our measurements (Fig. 2). Physiological membrane potential must therefore significantly modulate the kinetic barriers for metal transport (Fig. 11 B). Lastly, our results suggest that metal transport by DraNramp is not kinetically symmetric, as metal transport is much faster for influx than
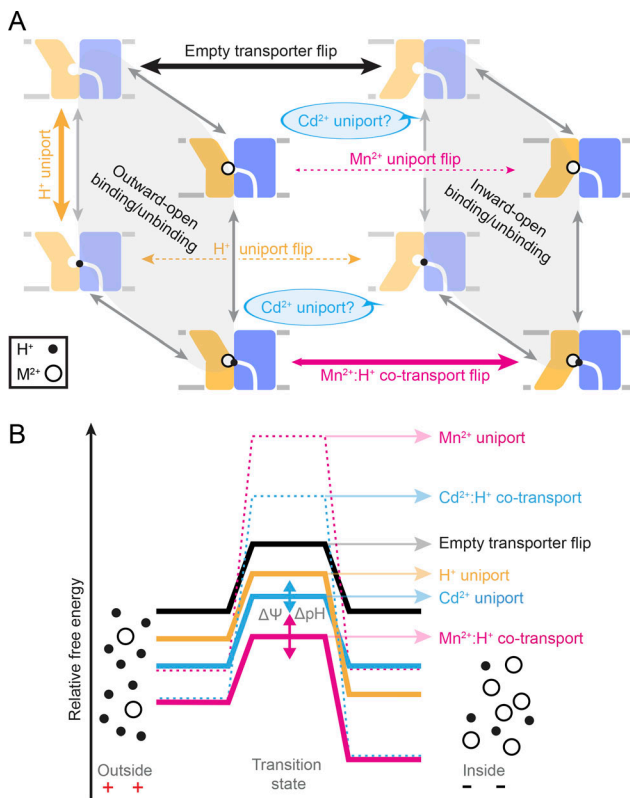
Bozzi et al.
Nramp M²⁺:H⁺ cotransport and uniport mechanisms

Journal of General Physiology 1424
https://doi.org/10.1085/jgp.201912428

Figure 11. **Kinetic model of DraNramp activity. (A)** Transport cycle diagram including all possible binding/unbinding events as well as all observed (solid lines) and hypothetical (dashed lines) transport events for DraNramp. While metal transport always requires bulk conformational change, proton uniport occurs through the outward-open state (Bozzi et al., 2019). Cd^{2+} uniport (horizontal cycles) could occur in the presence or absence of a bound proton. **(B)** Simplified, hypothetical free energy diagrams for DraNramp transport events in a typical physiological context of higher $[H^+]$ outside, higher $[M^{2+}]$ inside, and a moderate negative-inside $\Delta\Psi$. Proton cotransport may significantly reduce the barrier to Mn^{2+} transport, while Cd^{2+} uniport may instead have the lowest barrier under physiological conditions. Voltage affects both the magnitude of the energetic barriers for metal transport as well as the relative ΔG for transport, while ΔpH affects the energetic barrier and relative ΔG depending on the extent of thermodynamic coupling between metal and proton transport. The much faster rates seen for metal forward-transport over back-transport imply asymmetric kinetic barriers (and thus likely additional stable intermediate states), which are not shown in this model.

for efflux with the same thermodynamic driving force (Fig. 10).

To begin to understand how DraNramp's structure enables this noncanonical transport, we targeted the network of conserved protonatable residues that stretches from the metal-binding site to the cytosolic side of the membrane (Fig. 6). Single point mutations within this network reduced the voltage dependence (Fig. 7) and ΔpH dependence (Fig. 8) of metal transport rate, perturbed or eliminated metal-stimulated proton transport (Fig. 8), altered metal selectivity (Fig. 9), and enabled significant metal efflux to occur (Fig. 10). We summarize the results of these mutagenesis experiments in Table S1 and propose the following model as one plausible mechanism for Nramp manganese-proton cotransport (Fig. 12 A). D56 is first

protonated to optimally orient the metal-binding residues—donating a hydrogen bond to the metal-interacting N59 carbonyl oxygen rather than receiving a hydrogen bond from the amide nitrogen (Fig. 12 B)—a process facilitated by E134, M230, and H232. D56 protonation also neutralizes the protein core. Incoming Mn^{2+} displaces the H^+ from D56 and interacts with N59, the A53 carbonyl, and M230, which bonds semi-covalently to selectively stabilize the transition metal substrate. H232 and E134 may stabilize the H^+ in a transition state before it reaches D131, but they are not essential in other Nramp homologues for which neutralizing mutations at those positions preserve proton–metal cotransport behavior (Mackenzie et al., 2006; Ehrnstorfer et al., 2017). This H^+ transfer thus redistributes the net added positive charge, such that both the metal-binding site and the salt-bridge network gain a +1 formal charge. The metal binding and proton transfer trigger the bulk conformational change to bring the transporter to the inward-facing state, in which the external vestibule closes and the cytosolic vestibule opens to allow eventual Mn^{2+} release (Bozzi et al., 2019). The proton is released to the cytosol, likely through the salt-bridge network where numerous conserved hydrophilic residues and ordered waters may aid its passage. Proton uniport, which we previously showed does not require bulk conformational change from outward-to-inward facing state (Bozzi et al., 2019), follows the same pathway through the salt-bridge network. Additional protonation states during this process are possible, but the available mutagenesis data do not enable predictions as to their identity. Future experiments and molecular dynamics simulations may elucidate additional stable or intermediate protonation states. Additional mechanistic details remain to be determined such as the extent of thermodynamic coupling between the metal and proton, how metal substrate binding initiates conformational change, and if and how this conformational change affects H^+ movement through the salt-bridge network.

For DraNramp, the distinction between proton–metal cotransport (Mn^{2+}, Fe^{2+}, and Co^{2+}) and metal uniport (Zn^{2+} and Cd^{2+}) follows a familiar inorganic chemistry partition. The former cations have five, six, or seven valence d-electrons and typically prefer a coordination arrangement with more electron-donating ligands than do the latter metals which have a filled d-shell (Barber-Zucker et al., 2017). Therefore, while D56 coordinates Mn^{2+} in a bidentate manner requiring deprotonation (Fig. 12 D) as we modeled for DraNramp's outward-facing state (Bozzi et al., 2019), D56 may instead interact with Cd^{2+} only through its carbonyl oxygen and thus retain its proton (Fig. 12 C). The greater importance of M230 for Cd^{2+} than Mn^{2+} transport (Fig. 9, C and D; Bozzi et al., 2016a, 2019) further supports differential binding properties for the two metals. Our Mn^{2+} and H^+ cotransport results are consistent with in vitro findings with Mn^{2+} for *E. coleocola* Nramp (Ehrnstorfer et al., 2017). In contrast, the Cd^{2+} uniport we report contradicts in vivo results showing Cd^{2+} stimulates intracellular acidification in cells overexpressing *E. coli* Nramp (Courville et al., 2008), which has the same conserved salt-bridge network as DraNramp (Fig. 6). However, this study did not address the effects of Mn^{2+} or other metal substrates on intracellular pH. Furthermore, the inherent
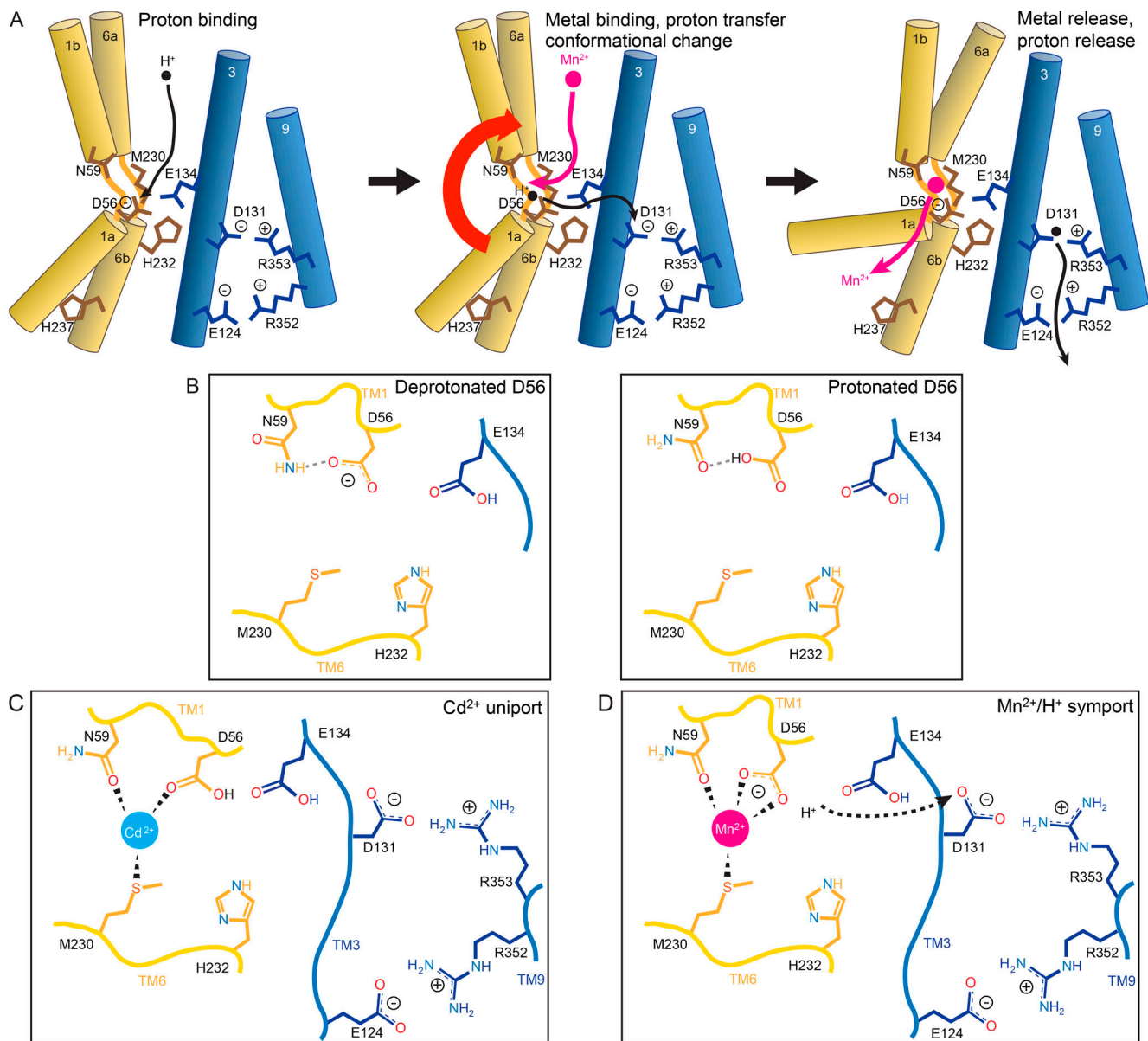
Figure 12. **Proposed DraNramp proton-metal cotransport mechanism. (A)** Proposed mechanism of proton-metal cotransport. Left: D56 protonation optimizes the metal-binding site via hydrogen bonding of D56 to the N59 carbonyl oxygen, providing a better metal-binding ligand than the amide nitrogen (as shown in B). Center: Metal substrate binds, displacing the D56 proton, which passes to D131, with H232 and E134 stabilizing a high-energy transition state and triggering bulk conformational change. Right: The proton exits to the cytosol via the TM3/TM9 salt-bridge network, while the metal is released into the cytosolic vestibule. **(B)** Detailed view of how protonation of D56 could alter the metal-binding site. **(C and D)** Cd^{2+} uniport perhaps occurs due to a mono-dentate interaction with D56, enabling proton retention. Bidentate binding of D56 by Mn^{2+} requires deprotonation, passing the proton to D131. See also Table S1.

complexity of such in vivo experiments compared with an artificial proteoliposome means that the observed intracellular pH changes were perhaps not due to flux through *E. coli* Nramp.

Intriguingly, perturbing either the metal-binding site or the adjoining salt-bridge network eliminates the H^+ cotransport distinction between Cd^{2+} and Mn^{2+} (Fig. 8, C and D). Cd^{2+} stimulated H^+ transport by the N59A and M230A variants, which suggests that in those variants D56 may compensate for the loss of a native metal ligand by interacting in a bidentate manner with Cd^{2+} and thus shedding a H^+. In addition, mutations at residues ≥ 15 Å from bound M^{2+} also upset this

distinction (i.e., both metals stimulate H^+ transport by the R352A variant, while E124A and R353A shift to uniport of both metals), further underscoring the long-range influence of the salt-bridge network.

Overall, our experiments with different metals and point mutations indicate two distinct roles for protons in DraNramp's mechanism: (i) ΔpH stimulation of metal transport rate, and (ii) metal stimulation of proton transport. Lower pH likely optimizes the metal-binding site via D56 protonation (Fig. 12 B), and mutations to residues in the immediate vicinity of D56 (M230, E134, H232) completely eliminate ΔpH dependence of transport

(Fig. 8, A and B), perhaps in part by shifting D56's pK_a. Intriguingly, ΔpH accelerates Cd^{2+} transport in WT and Mn^{2+} transport in proton-pathway mutants like D131A, although less than in WT. Complementarily, proton cotransport is still observed for mutants such as M230A that eliminate the effect of ΔpH but do not compromise the conserved proton-transport pathway (Bozzi et al., 2019). Therefore, a ΔpH effect on the uptake rate of primary substrate should not be conflated with H^+ cotransport and vice versa, whether in other Nramp homologues or unrelated secondary transporters.

Outside the Nramp family, proton–metal cotransport was demonstrated for the *E. coli* Zn^{2+} transporter ZntB (Gati et al., 2017), which belongs to the CorA metal ion transporter family, and the mouse Zn^{2+} transporter ZIP4 (Hoch and Sekler, 2018), a member of the Zrt/Irt-like protein (ZIP) family. In addition, proton–metal antiport was observed for a second *E. coli* Zn^{2+} transporter ZitB (Chao and Fu, 2004) and the human Zn^{2+} transporter ZnT5 (Ohana et al., 2009), both members of the cation diffusion facilitator family, as well as the *Cupriavidus metallidurans* Co^{2+}, Zn^{2+}, and Cd^{2+} transporter CzcA (Nies, 1995) from the heavy metal efflux resistance-nodulation-cell division (HME-RND) family. The ability to mechanistically intertwine proton and metal transport thus appears to have evolved independently in several different protein families with diverse structures, although the lack of details regarding how coupling is enforced in most cases renders it difficult to assess whether any mechanistic similarities exist.

The canonical model for secondary transport posits a cycle in which each transition is fully reversible, precise stoichiometry is maintained, and the prevailing ion gradients determine the directionality of net transport (Fig. 1). Effective symport thus requires tight coupling between the cosubstrates, which is implemented in transporters by the driving ions either structurally enabling binding of the primary substrate or mechanistically selectively stabilizing a certain conformational state (Perez and Ziegler, 2013; Rudnick, 2013). Indeed, for the LeuT amino acid transporter—a structural homologue of DraNramp—substrate binding depends on two bound Na^+ ions (Erlendsson et al., 2017): one Na^+ stabilizes the outward-open conformation (Claxton et al., 2010; Tavoulari et al., 2016) while a second Na^+ binds the transported amino acid's carboxylate (Yamashita et al., 2005).

DraNramp proton-metal cotransport deviates from basic principles of canonical symport. First, while Mn^{2+} was cotransported with H^+, uncoupled H^+ flux occurs readily in the absence of metal (Fig. 5), which may result in the variable cotransport stoichiometries previously reported for yeast and mammalian Nramp homologues (Chen et al., 1999; Mackenzie et al., 2006, 2007). These "futile cycles" are energetically wasteful, depleting ΔΨ and ΔpH without assisting in the uptake of the primary substrate. It is intriguing that evolution has retained such a thermodynamic cost as a general feature of the Nramp family, especially as simple tweaks near the salt-bridge network were shown to reduce H^+ uniport without impairing metal uptake (Nevo and Nelson, 2004). Second, because of their like charges it is energetically unfavorable for the two substrates to directly interact in the binding site during the transport process. Indeed, our

results suggest that H^+ transport and M^{2+} binding may actually become competitive processes under some conditions, underscoring the cosubstrate's imperfect synergy (Fig. 4). DraNramp's salt-bridge network may have evolved as a way of spatially separating the cationic metals and proton during the conformational change process. Thus, DraNramp may rely on a longer-range allosteric structural connection between the cosubstrates rather than a stable direct interaction like that seen in LeuT (Yamashita et al., 2005).

Our results also demonstrate a kinetic role for the physiological membrane potential in DraNramp metal transport (Fig. 2 and 4). Although such voltage dependence may be a diffuse property for a transport protein, our mutagenesis data show that neutralizing mutations within the conserved salt-bridge network lining DraNramp's ion transport routes alter the voltage dependence and increase transport at lower magnitude ΔΨ (Fig. 7). Thus, this Nramp-specific structural feature may impart a voltage-sensitive rate-limiting step to the transport process, although the details of this phenomenon remain to be determined. Of note, as the effects of Δψ, pH, and ΔpH are distinct for different metals, these properties likely affect steps in the transport cycle where the metal is bound, and the mechanistic details may thus vary for different metal substrates.

DraNramp's noncanonical proton-metal cotransport and strong voltage dependence may serve to make metal import essentially kinetically irreversible. Indeed, no Mn^{2+} transport occurs in the absence of a negative ΔΨ (Fig. 2; cations leaving the cell would experience an unfavorable [inside negative] ΔΨ). Furthermore, inside-out transporters—even with a favorable ΔΨ—fail to efficiently import Mn^{2+} into liposomes down a large concentration gradient (Fig. 10). The inward-to-outward metal-bound transition is thus essentially kinetically forbidden in the WT protein under physiological conditions. Strikingly, point mutations to the salt-bridge network that perturb voltage dependence, ΔpH dependence, and/or proton cotransport erode these restrictions, such that these protein variants behave more like directionally unbiased uniporters (Fig. 10). The unique features in DraNramp's structure may therefore have evolved to enforce a transport mechanism that, though energetically wasteful due to its propensity for proton uniport, is optimally adapted to the cellular context with robust safeguards against the back transport of precious intracellular metal stores.

Data availability

The raw biochemical data that support the findings of this study are available from the corresponding author upon reasonable request.

References

Abbaspour, N., R. Hurrell, and R. Kelishadi. 2014. Review on iron and its importance for human health. *J. Res. Med. Sci.* 19:164–174.

Agranoff, D., I.M. Monahan, J.A. Mangan, P.D. Butcher, and S. Krishna. 1999. Mycobacterium tuberculosis expresses a novel pH-dependent divalent cation transporter belonging to the Nramp family. *J. Exp. Med.* 190: 717–724. https://doi.org/10.1084/jem.190.5.717

Agranoff, D., L. Collins, D. Kehres, T. Harrison, M. Maguire, and S. Krishna. 2005. The Nramp orthologue of Cryptococcus neoformans is a pH-dependent transporter of manganese, iron, cobalt and nickel. *Biochem. J.* 385:225–232. https://doi.org/10.1042/BJ20040836

Andrews, N.C. 2008. Forging a field: the golden age of iron biology. *Blood.* 112: 219–230. https://doi.org/10.1182/blood-2007-12-077388

Bannon, D.I., M.E. Portnoy, L. Olivi, P.S.J. Lees, V.C. Culotta, and J.P. Bressler. 2002. Uptake of lead and iron by divalent metal transporter 1 in yeast and mammalian cells. *Biochem. Biophys. Res. Commun.* 295:978–984. https://doi.org/10.1016/S0006-291X(02)00756-8

Barber-Zucker, S., B. Shaanan, and R. Zarivach. 2017. Transition metal binding selectivity in proteins and its correlation with the phylogenomic classification of the cation diffusion facilitator protein family. *Sci. Rep.* 7:16381. https://doi.org/10.1038/s41598-017-16777-5

Bot, C.T., and C. Prodan. 2010. Quantifying the membrane potential during E. coli growth stages. *Biophys. Chem.* 146:133–137. https://doi.org/10.1016/j.bpc.2009.11.005

Boudker, O., and G. Verdon. 2010. Structural perspectives on secondary active transporters. *Trends Pharmacol. Sci.* 31:418–426. https://doi.org/10.1016/j.tips.2010.06.004

Bozzi, A.T., L.B. Bane, W.A. Weihofen, A.L. McCabe, A. Singharoy, C.J. Chipot, K. Schulten, and R. Gaudet. 2016a. Conserved methionine dictates substrate preference in Nramp-family divalent metal transporters. *Proc. Natl. Acad. Sci. USA.* 113:10310–10315. https://doi.org/10.1073/pnas.1607734113

Bozzi, A.T., L.B. Bane, W.A. Weihofen, A. Singharoy, E.R. Guillen, H.L. Ploegh, K. Schulten, and R. Gaudet. 2016b. Crystal Structure and Conformational Change Mechanism of a Bacterial Nramp-Family Divalent Metal Transporter. *Structure.* 24:2102–2114. https://doi.org/10.1016/j.str.2016.09.017

Bozzi, A.T., C.M. Zimanyi, J.M. Nicoludis, B.K. Lee, C.H. Zhang, and R. Gaudet. 2019. Structures in multiple conformations reveal distinct transition metal and proton pathways in an Nramp transporter. *eLife.* 8: e41124. https://doi.org/10.7554/eLife.41124

Bressler, J.P., L. Olivi, J.H. Cheong, Y. Kim, and D. Bannona. 2004. Divalent metal transporter 1 in lead and cadmium transport. *Ann. N. Y. Acad. Sci.* 1012:142–152. https://doi.org/10.1196/annals.1306.011

Buracco, S., B. Peracino, R. Cinquetti, E. Signoretto, A. Vollero, F. Imperiali, M. Castagna, E. Bossi, and S. Bozzaro. 2015. Dictyostelium Nramp1, which is structurally and functionally similar to mammalian DMT1 transporter, mediates phagosomal iron efflux. *J. Cell Sci.* 128:3304–3316. https://doi.org/10.1242/jcs.173153

Cailliatte, R., A. Schikora, J.F. Briat, S. Mari, and C. Curie. 2010. High-affinity manganese uptake by the metal transporter NRAMP1 is essential for Arabidopsis growth in low manganese conditions. *Plant Cell.* 22: 904–917. https://doi.org/10.1105/tpc.109.073023

Cellier, M.F.M. 2012. Nramp: from sequence to structure and mechanism of divalent metal import. *Curr. Top. Membr.* 69:249–293. https://doi.org/10.1016/B978-0-12-394390-3.00010-0

Cellier, M.F.M. 2016. Evolutionary analysis of Slc11 mechanism of proton-coupled metal-ion transmembrane import. *AIMS Biophys.* 3:286–318. https://doi.org/10.3934/biophy.2016.2.286

Chao, Y., and D. Fu. 2004. Kinetic study of the antiport mechanism of an Escherichia coli zinc transporter, ZitB. *J. Biol. Chem.* 279:12043–12050. https://doi.org/10.1074/jbc.M313510200

Chen, X.Z., J.B. Peng, A. Cohen, H. Nelson, N. Nelson, and M.A. Hediger. 1999. Yeast SMF1 mediates H(+)-coupled iron uptake with concomitant uncoupled cation currents. *J. Biol. Chem.* 274:35089–35094. https://doi.org/10.1074/jbc.274.49.35089

Claxton, D.P., M. Quick, L. Shi, F.D. de Carvalho, H. Weinstein, J.A. Javitch, and H.S. McHaourab. 2010. Ion/substrate-dependent conformational dynamics of a bacterial homolog of neurotransmitter:sodium symporters. *Nat. Struct. Mol. Biol.* 17:822–829. https://doi.org/10.1038/nsmb.1854

Coffey, R., and T. Ganz. 2017. Iron homeostasis: An anthropocentric perspective. *J. Biol. Chem.* 292:12727–12734. https://doi.org/10.1074/jbc.R117.781823

Courville, P., R. Chaloupka, and M.F. Cellier. 2006. Recent progress in structure-function analyses of Nramp proton-dependent metal-ion transporters. *Biochem. Cell Biol.* 84:960–978. https://doi.org/10.1139/o06-193

Courville, P., E. Urbankova, C. Rensing, R. Chaloupka, M. Quick, and M.F. Cellier. 2008. Solute carrier 11 cation symport requires distinct residues in transmembrane helices 1 and 6. *J. Biol. Chem.* 283:9651–9658. https://doi.org/10.1074/jbc.M709906200

Ehrnstorfer, I.A., E.R. Geertsma, E. Pardon, J. Steyaert, and R. Dutzler. 2014. Crystal structure of a SLC11 (NRAMP) transporter reveals the basis for transition-metal ion transport. *Nat. Struct. Mol. Biol.* 21:990–996. https://doi.org/10.1038/nsmb.2904

Ehrnstorfer, I.A., C. Manatschal, F.M. Arnold, J. Laederach, and R. Dutzler. 2017. Structural and mechanistic basis of proton-coupled metal ion transport in the SLC11/NRAMP family. *Nat. Commun.* 8:14033. https://doi.org/10.1038/ncomms14033

Erlendsson, S., K. Gotfryd, F.H. Larsen, J.S. Mortensen, M.A. Geiger, B.J. van Rossum, H. Oschkinat, U. Gether, K. Teilum, and C.J. Loland. 2017. Direct assessment of substrate binding to the Neurotransmitter:Sodium Symporter LeuT by solid state NMR. *eLife.* 6:e19314. https://doi.org/10.7554/eLife.19314

Fleming, M.D., C.C. Trenor III, M.A. Su, D. Foernzler, D.R. Beier, W.F. Dietrich, and N.C. Andrews. 1997. Microcytic anaemia mice have a mutation in Nramp2, a candidate iron transporter gene. *Nat. Genet.* 16: 383–386. https://doi.org/10.1038/ng0897-383

Fleming, M.D., M.A. Romano, M.A. Su, L.M. Garrick, M.D. Garrick, and N.C. Andrews. 1998. Nramp2 is mutated in the anemic Belgrade (b) rat: evidence of a role for Nramp2 in endosomal iron transport. *Proc. Natl. Acad. Sci. USA.* 95:1148–1153. https://doi.org/10.1073/pnas.95.3.1148

Forbes, J.R., and P. Gros. 2003. Iron, manganese, and cobalt transport by Nramp1 (Slc11a1) and Nramp2 (Slc11a2) expressed at the plasma membrane. *Blood.* 102:1884–1892. https://doi.org/10.1182/blood-2003-02-0425

Forrest, L.R., R. Krämer, and C. Ziegler. 2011. The structural basis of secondary active transport mechanisms. *Biochim. Biophys. Acta.* 1807: 167–188. https://doi.org/10.1016/j.bbabio.2010.10.014

Gadsby, D.C. 2009. Ion channels versus ion pumps: the principal difference, in principle. *Nat. Rev. Mol. Cell Biol.* 10:344–352. https://doi.org/10.1038/nrm2668

Gati, C., A. Stetsenko, D.J. Slotboom, S.H.W. Scheres, and A. Guskov. 2017. The structural basis of proton driven zinc transport by ZntB. *Nat. Commun.* 8:1313. https://doi.org/10.1038/s41467-017-01483-7

Grynkiewicz, G., M. Poenie, and R.Y. Tsien. 1985. A new generation of Ca2+ indicators with greatly improved fluorescence properties. *J. Biol. Chem.* 260:3440–3450.

Gunshin, H., B. Mackenzie, U.V. Berger, Y. Gunshin, M.F. Romero, W.F. Boron, S. Nussberger, J.L. Gollan, and M.A. Hediger. 1997. Cloning and characterization of a mammalian proton-coupled metal-ion transporter. *Nature.* 388:482–488. https://doi.org/10.1038/41343

Haemig, H.A., and R.J. Brooker. 2004. Importance of conserved acidic residues in mntH, the Nramp homolog of Escherichia coli. *J. Membr. Biol.* 201:97–107. https://doi.org/10.1007/s00232-004-0711-x

Haemig, H.A., P.J. Moen, and R.J. Brooker. 2010. Evidence that highly conserved residues of transmembrane segment 6 of Escherichia coli MntH

are important for transport activity. *Biochemistry.* 49:4662–4671. https://doi.org/10.1021/bi100320y

Henderson, R.K., K. Fendler, and B. Poolman. 2019. Coupling efficiency of secondary active transporters. *Curr. Opin. Biotechnol.* 58:62–71. https://doi.org/10.1016/j.copbio.2018.11.005

Hinkle, P.M., E.D. Shanshala II, and E.J. Nelson. 1992. Measurement of intracellular cadmium with fluorescent dyes. Further evidence for the role of calcium channels in cadmium uptake. *J. Biol. Chem.* 267:25553–25559.

Hoch, E., and I. Sekler. 2018. Elucidating the H+ coupled Zn2+ transport mechanism of ZIP; implications in Acrodermatitis enteropathica. *BioRxiv. Preprint.* November 20, 2018.

Hood, M.I., and E.P. Skaar. 2012. Nutritional immunity: transition metals at the pathogen-host interface. *Nat. Rev. Microbiol.* 10:525–537. https://doi.org/10.1038/nrmicro2836

Illing, A.C., A. Shawki, C.L. Cunningham, and B. Mackenzie. 2012. Substrate profile and metal-ion selectivity of human divalent metal-ion transporter-1. *J. Biol. Chem.* 287:30485–30496. https://doi.org/10.1074/jbc.M112.364208

Iolascon, A., M. d'Apolito, V. Servedio, F. Cimmino, A. Piga, and C. Camaschella. 2006. Microcytic anemia and hepatic iron overload in a child with compound heterozygous mutations in DMT1 (SCL11A2). *Blood.* 107:349–354. https://doi.org/10.1182/blood-2005-06-2477

Kehres, D.G., M.L. Zaharik, B.B. Finlay, and M.E. Maguire. 2000. The NRAMP proteins of Salmonella typhimurium and Escherichia coli are selective manganese transporters involved in the response to reactive oxygen. *Mol. Microbiol.* 36:1085–1100. https://doi.org/10.1046/j.1365-2958.2000.01922.x

Lam-Yuk-Tseung, S., G. Govoni, J. Forbes, and P. Gros. 2003. Iron transport by Nramp2/DMT1: pH regulation of transport by 2 histidines in transmembrane domain 6. *Blood.* 101:3699–3707. https://doi.org/10.1182/blood-2002-07-2108

Lam-Yuk-Tseung, S., C. Camaschella, A. Iolascon, and P. Gros. 2006. A novel R416C mutation in human DMT1 (SLC11A2) displays pleiotropic effects on function and causes microcytic anemia and hepatic iron overload. *Blood Cells Mol. Dis.* 36:347–354. https://doi.org/10.1016/j.bcmd.2006.01.011

Lan, W., H. Ren, Y. Pang, C. Huang, Y. Xu, R.J. Brooker, and J. Zhang. 2012. A facile transport assay for H+coupled membrane transport using fluorescence probes. *Anal. Methods.* 4:44–46. https://doi.org/10.1039/C1AY05549F

LeVine, M.V., M.A. Cuendet, G. Khelashvili, and H. Weinstein. 2016. Allosteric Mechanisms of Molecular Machines at the Membrane: Transport by Sodium-Coupled Symporters. *Chem. Rev.* 116:6552–6587. https://doi.org/10.1021/acs.chemrev.5b00627

Loo, D.D.F., B.A. Hirayama, E.M. Gallardo, J.T. Lam, E. Turk, and E.M. Wright. 1998. Conformational changes couple Na+ and glucose transport. *Proc. Natl. Acad. Sci. USA.* 95:7789–7794. https://doi.org/10.1073/pnas.95.13.7789

Ma, Z., F.E. Jacobsen, and D.P. Giedroc. 2009. Coordination chemistry of bacterial metal transport and sensing. *Chem. Rev.* 109:4644–4681. https://doi.org/10.1021/cr900077w

Mackenzie, B., and M.A. Hediger. 2004. SLC11 family of H+-coupled metal-ion transporters NRAMP1 and DMT1. *Pflugers Arch.* 447:571–579. https://doi.org/10.1007/s00424-003-1141-9

Mackenzie, B., M.L. Ujwal, M.H. Chang, M.F. Romero, and M.A. Hediger. 2006. Divalent metal-ion transporter DMT1 mediates both H+-coupled Fe2+ transport and uncoupled fluxes. *Pflugers Arch.* 451:544–558. https://doi.org/10.1007/s00424-005-1494-3

Mackenzie, B., H. Takanaga, N. Hubert, A. Rolfs, and M.A. Hediger. 2007. Functional properties of multiple isoforms of human divalent metal-ion transporter 1 (DMT1). *Biochem. J.* 403:59–69. https://doi.org/10.1042/BJ20061290

Makui, H., E. Roig, S.T. Cole, J.D. Helmann, P. Gros, and M.F.M. Cellier. 2000. Identification of the Escherichia coli K-12 Nramp orthologue (MntH) as a selective divalent metal ion transporter. *Mol. Microbiol.* 35:1065–1078. https://doi.org/10.1046/j.1365-2958.2000.01774.x

Nelson, N., A. Sacher, and H. Nelson. 2002. The significance of molecular slips in transport systems. *Nat. Rev. Mol. Cell Biol.* 3:876–881. https://doi.org/10.1038/nrm955

Nevo, Y., and N. Nelson. 2004. The mutation F227I increases the coupling of metal ion transport in DCT1. *J. Biol. Chem.* 279:53056–53061. https://doi.org/10.1074/jbc.M408398200

Nevo, Y., and N. Nelson. 2006. The NRAMP family of metal-ion transporters. *Biochim. Biophys. Acta.* 1763:609–620. https://doi.org/10.1016/j.bbamcr.2006.05.007

Nies, D.H. 1995. The cobalt, zinc, and cadmium efflux system CzcABC from Alcaligenes eutrophus functions as a cation-proton antiporter in Escherichia coli. *J. Bacteriol.* 177:2707–2712. https://doi.org/10.1128/jb.177.10.2707-2712.1995

Ohana, E., E. Hoch, C. Keasar, T. Kambe, O. Yifrach, M. Hershfinkel, and I. Sekler. 2009. Identification of the Zn2+ binding site and mode of operation of a mammalian Zn2+ transporter. *J. Biol. Chem.* 284:17677–17686. https://doi.org/10.1074/jbc.M109.007203

Perez, C., and C. Ziegler. 2013. Mechanistic aspects of sodium-binding sites in LeuT-like fold symporters. *Biol. Chem.* 394:641–648. https://doi.org/10.1515/hsz-2012-0336

Picard, V., G. Govoni, N. Jabado, and P. Gros. 2000. Nramp 2 (DCT1/DMT1) expressed at the plasma membrane transports iron and other divalent cations into a calcein-accessible cytoplasmic pool. *J. Biol. Chem.* 275:35738–35745. https://doi.org/10.1074/jbc.M005387200

Pujol-Giménez, J., M.A. Hediger, and G. Gyimesi. 2017. A novel proton transfer mechanism in the SLC11 family of divalent metal ion transporters. *Sci. Rep.* 7:6194. https://doi.org/10.1038/s41598-017-06446-y

Rudnick, G. 2013. How do transporters couple solute movements? *Mol. Membr. Biol.* 30:355–359. https://doi.org/10.3109/09687688.2013.842658

Sacher, A., A. Cohen, and N. Nelson. 2001. Properties of the mammalian and yeast metal-ion transporters DCT1 and Smf1p expressed in Xenopus laevis oocytes. *J. Exp. Biol.* 204:1053–1061.

Shabala, L., J. Bowman, J. Brown, T. Ross, T. McMeekin, and S. Shabala. 2009. Ion transport and osmotic adjustment in Escherichia coli in response to ionic and non-ionic osmotica. *Environ. Microbiol.* 11:137–148. https://doi.org/10.1111/j.1462-2920.2008.01748.x

Shawki, A., and B. Mackenzie. 2010. Interaction of calcium with the human divalent metal-ion transporter-1. *Biochem. Biophys. Res. Commun.* 393:471–475. https://doi.org/10.1016/j.bbrc.2010.02.025

Shawki, A., P.B. Knight, B.D. Maliken, E.J. Niespodzany, and B. Mackenzie. 2012. H(+)-coupled divalent metal-ion transporter-1: functional properties, physiological roles and therapeutics. *Curr. Top. Membr.* 70:169–214. https://doi.org/10.1016/B978-0-12-394316-3.00005-3

Shi, Y. 2013. Common folds and transport mechanisms of secondary active transporters. *Annu. Rev. Biophys.* 42:51–72. https://doi.org/10.1146/annurev-biophys-083012-130429

Shilton, B.H. 2015. Active transporters as enzymes: an energetic framework applied to major facilitator superfamily and ABC importer systems. *Biochem. J.* 467:193–199. https://doi.org/10.1042/BJ20140675

Su, M.A., C.C. Trenor, J.C. Fleming, M.D. Fleming, and N.C. Andrews. 1998. The G185R mutation disrupts function of the iron transporter Nramp2. *Blood.* 92:2157–2163.

Supek, F., L. Supekova, H. Nelson, and N. Nelson. 1996. A yeast manganese transporter related to the macrophage protein involved in conferring resistance to mycobacteria. *Proc. Natl. Acad. Sci. USA.* 93:5105–5110. https://doi.org/10.1073/pnas.93.10.5105

Tandy, S., M. Williams, A. Leggett, M. Lopez-Jimenez, M. Dedes, B. Ramesh, S.K. Srai, and P. Sharp. 2000. Nramp2 expression is associated with pH-dependent iron uptake across the apical membrane of human intestinal Caco-2 cells. *J. Biol. Chem.* 275:1023–1029. https://doi.org/10.1074/jbc.275.2.1023

Tavoulari, S., E. Margheritis, A. Nagarajan, D.C. DeWitt, Y.-W. Zhang, E. Rosado, S. Ravera, E. Rhoades, L.R. Forrest, and G. Rudnick. 2016. Two Na+ Sites Control Conformational Change in a Neurotransmitter Transporter Homolog. *J. Biol. Chem.* 291:1456–1471. https://doi.org/10.1074/jbc.M115.692012

Thomine, S., R. Wang, J.M. Ward, N.M. Crawford, and J.I. Schroeder. 2000. Cadmium and iron transport by members of a plant metal transporter family in Arabidopsis with homology to Nramp genes. *Proc. Natl. Acad. Sci. USA.* 97:4991–4996. https://doi.org/10.1073/pnas.97.9.4991

Vázquez, M., D. Vélez, V. Devesa, and S. Puig. 2015. Participation of divalent cation transporter DMT1 in the uptake of inorganic mercury. *Toxicology.* 331:119–124. https://doi.org/10.1016/j.tox.2015.03.005

Xu, H., J. Jin, L.J. DeFelice, N.C. Andrews, and D.E. Clapham. 2004. A spontaneous, recurrent mutation in divalent metal transporter-1 exposes a calcium entry pathway. *PLoS Biol.* 2:E50. https://doi.org/10.1371/journal.pbio.0020050

Yamashita, A., S.K. Singh, T. Kawate, Y. Jin, and E. Gouaux. 2005. Crystal structure of a bacterial homologue of Na+/Cl--dependent neurotransmitter transporters. *Nature.* 437:215–223. https://doi.org/10.1038/nature03978